Eur. Phys. J. E (2010)
DOI 10.1140/epje/i2010-10610-7

THE EUROPEAN PHYSICAL JOURNAL E

Regular Article

Viscous compressible hydrodynamics at planes, spheres and cylinders with finite surface slip

A. Erbaş[1,a], R. Podgornik[2], and R.R. Netz[1]

[1] Physics Department, Technical University Munich, 85748 Garching, Germany
[2] IJS, Jamova 39, SI-1000 Ljubljana, Slovenia

Received 27 November 2009 and Received in final form 29 April 2010

Abstract. We consider the linearized time-dependent Navier-Stokes equation including finite compressibility and viscosity. We first constitute the Green's function, from which we derive the flow profiles and response functions for a plane, a sphere and a cylinder for arbitrary surface slip length. For high driving frequency the flow pattern is dominated by the diffusion of vorticity and compression, for low frequency compression propagates in the form of sound waves which are exponentially damped at a screening length larger than the sound wave length. The crossover between the diffusive and propagative compression regimes occurs at the fluid's intrinsic frequency $\omega \sim c^2\rho_0/\eta$, with c the speed of sound, ρ_0 the fluid density and η the viscosity. In the propagative regime the hydrodynamic response function of spheres and cylinders exhibits a high-frequency resonance when the particle size is of the order of the sound wave length. A distinct low-frequency resonance occurs at the boundary between the propagative and diffusive regimes. Those resonant features should be detectable experimentally by tracking the diffusion of particles, as well as by measuring the fluctuation spectrum or the response spectrum of trapped particles. Since the response function depends sensitively on the slip length, in principle the slip length can be deduced from an experimentally measured response function.

1 Introduction

In the last decade, microrheology, which uses micron-sized particles to probe the local dynamic response to applied forces, has become a useful tool to investigate the viscoelastic behavior of complex fluids such as biopolymer solutions, composites and complex interfaces [1,2]. Alternatively, the thermal mean displacement of spheres obtained from diffusing wave spectroscopy, interferometry, laser deflection or video-tracking is connected to the response function via the dissipation-fluctuation theorem and essentially yields equivalent information on the linear response level [3–6]. Likewise, ferromagnetic nanowires driven by external magnetic fields have been used to investigate anisotropic features of complex fluids and interfaces [7]. Knowing the hydrodynamic forces acting on small cylinders is also important for the development of advanced sensors and actuators [8–10]. In many applications, the Stokes' equation for an incompressible fluid with the no-slip boundary condition is used, but it was recognized early on that compressibility effects are crucial to describe certain phenomena [11–13]. In addition, a finite slip length, which is in the nanometer range for planar hydrophobic surfaces [14] and for curved objects shows an intricate dependence on flow direction and flow speed [15,16], can have drastic effects on the dynamics of nanometer size objects and thus has to be included in the treatment as well.

Based on the classical work by Stokes on the time-dependent response function for a sphere in a viscous incompressible medium [17,18], several works reported the response function for a finite-size sphere including slip and compressibility [19–22], but the explicit flow field has not been given. For the cylindrical case, compressibility has not been considered at all [23,24]. In the previous interpretation of microrheology measurements of complex fluids such as entangled polymer solutions, the dynamic response function of water has typically been considered featureless. In this paper we analyze the response function and flow profiles of a viscous compressible fluid at the basic geometries such as planes, spheres, cylinders in detail and show that the resulting behavior is quite rich, exhibiting resonant behavior both in the propagative as well as in the diffusive regime. Knowing the response function in principle allows to extract the slip length from experimentally measured spectral properties. The flow profile is important in situations where the hydrodynamic interaction between oscillating spheres or cylinders is probed and can help to rationalize hydrodynamic effects in confinement [25]. In addition, flows can be explicitly visualized with modern

[a] e-mail: aerbas@ph.tum.de

Published online: 25 June 0192

particle-image-velocimetry techniques, which would allow a direct comparison between theoretical and experimental results.

We first calculate the Green's function for a point force as a function of frequency in a compressible viscous fluid. Although this Green's function has been derived and used before, its explicit form is difficult to find in the literature and we therefore discuss it in some detail. Next, the flow fields at a plane, sphere and a cylinder are constructed for arbitrary surface slip length and the frequency-dependent response functions are derived by calculating the surface stress. The asymptotic behavior of the response functions as well as their resonant features are discussed in detail.

2 Constitutive equations

Conservation of the i-th component of the momentum in an arbitrary finite volume V reads

$$\frac{\mathrm{d}}{\mathrm{d}t}\int_V \rho v_i \mathrm{d}^3 r + \int_{\partial V} \rho v_i v_j \mathrm{d}f_j = \int_V F_i \mathrm{d}^3 r + \int_{\partial V} \Pi_{ij}\mathrm{d}f_j, \tag{1}$$

where density ρ, velocity v_i, volume force F_i, stress tensor Π_{ij} are functions of both time t and position $\mathbf{r}$, *i.e.* $\rho(\mathbf{r},t)$, $v_i(\mathbf{r},t)$, $F_i(\mathbf{r},t)$, $\Pi_{ij}(\mathbf{r},t)$, and the Einstein summation convention is used throughout this paper. Using Gauss law, the local momentum conservation follows as

$$\frac{\partial \rho v_i}{\partial t} + \nabla_j \rho v_i v_j = F_i + \nabla_j \Pi_{ij}. \tag{2}$$

With the help of the continuity equation, $\partial\rho/\partial t + \nabla_j \rho v_j = 0$ and the material derivative acting on an arbitrary scalar field $A(\mathbf{r},t)$, defined as $DA/Dt = \partial A/\partial t + v_i\nabla_i A$, the Navier-Stokes equation in compact notation results

$$\rho\frac{Dv_i}{Dt} = F_i + \nabla_j \Pi_{ij}. \tag{3}$$

The symmetric stress tensor is divided into the diagonal pressure contribution and a part that depends on velocity gradients $\nabla_j v_i$. To lowest order, which defines a Newtonian liquid, one obtains

$$\Pi_{ij} + p\delta_{ij} = \zeta\delta_{ij}\nabla_k v_k + \eta\left(\nabla_i v_j + \nabla_j v_i - \frac{2}{3}\delta_{ij}\nabla_k v_k\right), \tag{4}$$

where η is the shear viscosity and ζ denotes the volume viscosity, which is often set to zero. The Navier Stokes equation becomes

$$\rho\frac{Dv_i}{Dt} = F_i - \nabla_i p + (\eta/3+\zeta)\nabla_i\nabla_k v_k + \eta\nabla_k\nabla_k v_i. \tag{5}$$

Let us start out by a brief scaling analysis: Introducing scales for time, length, velocity, and density, T, L, V, ρ_0, respectively, and dividing the Navier-Stokes equation by $\eta V/L^2$ so that the viscosity terms are of order unity, the non-linear velocity term scales as the Reynolds number $\mathcal{R} \sim \rho_0 LV/\eta$, and the time-derivative term scales as $\mathcal{RST} \sim \rho_0 L^2/(\eta T)$. The Strouhal number is defined as $\mathcal{ST} \sim L/(VT)$ and measures the importance of the time derivative term compared to the non-linear term. Assuming water density $\rho_0 \simeq 10^3\,\mathrm{kg/m^3}$, water viscosity $\eta \simeq 10^{-3}\,\mathrm{kg/(m\,s)}$, and typical length and velocity scales for biological or colloidal systems in the micron range, $L \simeq 10^{-6}\,\mathrm{m}$, $V \simeq 10^{-6}\,\mathrm{m/s}$, the Reynolds number is $\mathcal{R} \simeq 10^{-6}$ and thus the non-linear term is negligible for such situations. The Strouhal number on the other hand can be quite large, depending on the time scale considered. Assuming a time scale $T \simeq 10^{-6}\,\mathrm{s}$, that means frequencies in the MHz range, the Strouhal number becomes $\mathcal{ST} \simeq 10^6$ and the time derivative term scales of the order of unity, $\mathcal{RST} \simeq 1$, and thus cannot be neglected. Such short times scales are important in a number of situations. By neglecting the non-linear term but keeping the time derivative, we are led to the so-called transient Stokes equation,

$$\rho\frac{\partial v_i}{\partial t} = F_i - \nabla_i p + (\eta/3+\zeta)\nabla_i\nabla_k v_k + \eta\nabla_k\nabla_k v_i, \tag{6}$$

which serves as the starting point for all further investigations in this paper. This equation is discussed in classical texts in the incompressible regime, where the term proportional to $\nabla_k v_k$ is absent [17]. For the case of finite compressibility only few and quite recent studies have been reported [19–22].

In the next section we first calculate the Green's function of the transient Stokes equation (6). The Green's function includes compression and shear effects, both are damped (or screened) beyond frequency-dependent length scales. Interestingly, for water the screening length of compression waves (sound waves) is for typical kHz frequencies in the kilometer range and thus much larger than the wave length, *i.e.*, compressional perturbations propagate. For much higher frequencies, the compression screening length becomes of the order of the wavelength and compression perturbations do not propagate. The screening length of shear or vortex diffusion is always of the order of the perturbation wavelength and thus shear perturbations never propagate. From the Green's function we construct the flow field at a plane, around a sphere and at a cylinder, using a generalized hydrodynamic boundary condition that includes a finite slip length b. We determine the pressure field and surface stress from which the forces acting on the bodies are derived. We find resonant features in the response functions, the scaling of which is analyzed in detail.

3 Calculation of the Green's function

On the linear level we treat v_i, $\rho-\rho_0$, $p-p_0$, F_i as small quantities. Taking the divergence of the Stokes equation (6), one obtains on the linear level

$$\nabla_i\nabla_i p - \frac{\partial^2 p}{c^2\partial t^2} = \nabla_i F_i + (4\eta/3+\zeta)\nabla_i\nabla_i\nabla_k v_k. \tag{7}$$

In deriving this we have used the linearized continuity equation, $\rho_0\nabla_i(\partial v_i/\partial t) = -\partial^2\rho/\partial t^2$ and the linearized equation of state $\rho - \rho_0 = c^{-2}(p - p_0)$, where $\mathrm{d}\rho/\mathrm{d}p|_{p_0} = c^{-2}$ defines the speed of sound c, from which follows $\partial^2\rho/\partial t^2 = c^{-2}\partial^2 p/\partial t^2$. Note that for most systems and frequencies, heat flow can be neglected so that the adiabatic limit is realized, though we hasten to stress that the linear theory as discussed here is independent of heat flow and dissipation effects. We define Fourier transforms as

$$p(\mathbf{r}, t) = \frac{1}{(2\pi)^4} \int \mathrm{d}\omega \mathrm{d}^3 k \tilde{p}(\mathbf{k}, \omega) e^{\imath(k_i r_i - \omega t)} \tag{8}$$

and similarly for v_i and F_i. Equations (6) and (7) become

$$-\imath\omega\rho_0 \tilde{v}_i = \tilde{F}_i - \imath k_i \tilde{p} - (\eta/3 + \zeta) k_i k_j \tilde{v}_j - \eta k_j k_j \tilde{v}_i \tag{9}$$

and

$$\left(\frac{\omega^2}{c^2} - k_i k_i\right) \tilde{p} = \imath k_i \tilde{F}_i - \imath(4\eta/3 + \zeta) k_i k_i k_j \tilde{v}_j. \tag{10}$$

Equation (10) allows to express the pressure field in terms of the velocity field. Thus eliminating the pressure term in eq. (9), one obtains an equation that only depends on velocity and external force. Straightforward solution of this algebraic equation is possible by decomposition of the velocity according to

$$\tilde{v}_i = \tilde{v}_i^T + \tilde{v}_i^L \tag{11}$$

into a transverse part defined by $k_i \tilde{v}_i^T = 0$ and a longitudinal part characterized by $k_i \tilde{v}_i = k_i \tilde{v}_i^L$. We define Green's functions for the transverse and longitudinal velocities as

$$\tilde{v}_i^T = \tilde{G}_{ij}^T \tilde{F}_j, \tag{12}$$

and

$$\tilde{v}_i^L = \tilde{G}_{ij}^L \tilde{F}_j. \tag{13}$$

The transverse Green's function describes the velocity field in the incompressible case and captures vorticity or shear effects; it has been derived by Stokes [17,18] and is given by

$$\tilde{G}_{ij}^T = \frac{(\delta_{ij} - k_i k_j / k^2)/\eta}{k^2 + \alpha^2}, \tag{14}$$

where we have defined the length scale α^{-1} via

$$\alpha^2 = -\imath\omega\rho_0/\eta. \tag{15}$$

On the other hand, the longitudinal Green's function describes compression effects and reads

$$\tilde{G}_{ij}^L = \frac{k_i k_j \lambda^2}{\eta\alpha^2 k^2 (k^2 + \lambda^2)}, \tag{16}$$

where we have defined the length scale λ^{-1} via

$$\lambda^2 = \frac{-\imath\omega\rho_0}{4\eta/3 + \zeta + \imath\rho_0 c^2/\omega}. \tag{17}$$

The complete Green's function is defined by

$$\tilde{v}_i = \tilde{G}_{ij} \tilde{F}_j \tag{18}$$

and is obtained from the sum of transverse and longitudinal Green's functions

$$\tilde{G}_{ij} = \tilde{G}_{ij}^T + \tilde{G}_{ij}^L. \tag{19}$$

3.1 Transverse Green's function

The transverse frequency-dependent Green's function in real space is obtained by straightforward back-fourier transformation and reads

$$\begin{aligned} G_{ij}^T = \frac{1}{4\pi\eta\alpha^2 r^3} \big\{ &\delta_{ij} \left([1 + r\alpha + r^2\alpha^2] e^{-r\alpha} - 1 \right) \\ &+ 3\hat{r}_i \hat{r}_j \left(1 - [1 + r\alpha + r^2\alpha^2/3] e^{-r\alpha} \right) \big\}. \end{aligned} \tag{20}$$

Note that eq. (20) is identical to Green's functions that are obtained for porous media [26]. For short distances, high viscosity or small frequencies, $r\alpha \ll 1$, the limiting behavior is

$$G_{ij}^T \simeq \frac{1}{8\pi\eta r} \left(\delta_{ij} + \hat{r}_i \hat{r}_j \right) \tag{21}$$

and corresponds to the static incompressible Green's function, the standard Oseen tensor [18]. For large distances or high frequencies, $r\alpha \gg 1$, corresponding to the inviscous case, the limiting behavior is

$$G_{ij}^T \simeq \frac{1}{4\pi\eta r^3 \alpha^2} \left(3\hat{r}_i \hat{r}_j - \delta_{ij} \right) \tag{22}$$

and exhibits a much faster decay (note that to leading order, the dependence on viscosity has dropped out). The decay constant α is separated into real and imaginary parts as

$$\alpha = \alpha_R + \imath\alpha_I. \tag{23}$$

By introducing the typical length scale a we obtain

$$a\alpha_R = -a\alpha_I = \sqrt{\omega/2\omega_0}, \tag{24}$$

where we have defined the vorticity frequency scale ω_0 as

$$\omega_0 = \frac{\eta}{a^2\rho_0}. \tag{25}$$

The inverse frequency ω_0^{-1} is the time that vorticity needs to diffuse a certain distance a. For water with density $\rho_0 \approx 10^3\,\mathrm{kg/m^3}$ and viscosity $\eta \approx 10^{-3}\,\mathrm{kg/m\,s}$, ω_0 ranges from $\omega_0 \simeq 1\,\mathrm{s^{-1}}$ for $a \simeq 1\,\mathrm{mm}$ to $\omega_0 \simeq 10^6\,\mathrm{s^{-1}}$ for $a \simeq 1\,\mu\mathrm{m}$. In water, the decay length scales as $\alpha_R^{-1} \simeq 10^{-3}(\omega\,\mathrm{s})^{-1/2}\,\mathrm{m}$ and thus is of the order of $\alpha_R^{-1} \simeq 1\,\mathrm{mm}$ for a frequency $\omega = 1\,\mathrm{s^{-1}}$ and $\alpha_R^{-1} \simeq 1\,\mu\mathrm{m}$ for a frequency $\omega = 10^6\,\mathrm{s^{-1}}$.

3.2 Longitudinal Green's function

The longitudinal Green's function in real space reads

$$\begin{aligned} G_{ij}^L = \frac{1}{4\pi\eta\alpha^2 r^3} \big\{ &\delta_{ij} \left(1 - [1 + r\lambda] e^{-r\lambda} \right) \\ &- 3\hat{r}_i \hat{r}_j \left(1 - [1 + r\lambda + r^2\lambda^2/3] e^{-r\lambda} \right) \big\}. \end{aligned} \tag{26}$$

For short distances, low compressibility (*i.e.* high sound speed) or small frequencies, $r\lambda \ll 1$, the limiting behavior is

$$G_{ij}^L \simeq \frac{\lambda^2}{8\pi\eta r\alpha^2} \left(\delta_{ij} - \hat{r}_i \hat{r}_j \right). \tag{27}$$

In the incompressible case, characterized by an infinite sound velocity, $c \to \infty$, one has $\lambda \to 0$ and thus the longitudinal Green's function vanishes. For large distances or high frequencies, $r\lambda \gg 1$, the limiting behavior is

$$G_{ij}^L \simeq -\frac{1}{4\pi\eta r^3\alpha^2}\left(3\hat{r}_i\hat{r}_j - \delta_{ij}\right) \tag{28}$$

and thus exactly cancels the asymptotic term from the incompressible Green's function given in eq. (22); the large-distance behavior of the total Green's function is thus determined by the next-leading-order terms and will be discussed in the next section. The decay constant λ is separated into real and imaginary parts as $\lambda = \lambda_R + \imath\lambda_I$, where

$$a\lambda_R = \frac{\omega}{\omega_0}\sqrt{\frac{\sqrt{1+[\omega/(\omega_0\gamma)(4/3+\zeta/\eta)]^2}-1}{2\gamma(1+[\omega/(\omega_0\gamma)(4/3+\zeta/\eta)]^2)}} \tag{29}$$

and

$$a\lambda_I = -\frac{\omega}{\omega_0}\sqrt{\frac{\sqrt{1+[\omega/(\omega_0\gamma)(4/3+\zeta/\eta)]^2}+1}{2\gamma(1+[\omega/(\omega_0\gamma)(4/3+\zeta/\eta)]^2)}} \tag{30}$$

and we have defined the dimensionless parameter

$$\gamma = \frac{c^2}{a^2\omega_0^2} = \left(\frac{a\rho_0 c}{\eta}\right)^2. \tag{31}$$

Noting that a/c is the typical compression time scale associated with the time in which a propagating sound wave travels a distance a, γ turns out to be the squared ratio of the vorticity time scale ω_0^{-1} and the compression time scale a/c. Besides the volume viscosity ζ, the vorticity frequency scale ω_0 and the length scale a, γ is the only remaining parameter. The asymptotic behavior of the real and imaginary parts of λ are

$$a\lambda_R = \begin{cases} 2/3(\omega/\omega_0)^2\gamma^{-3/2} - \mathcal{O}[(\omega/\omega_0)^4], & \text{for } \omega/(\omega_0\gamma) \ll 1, \\ \sqrt{3/8}(\omega/\omega_0)^{1/2} - \mathcal{O}[(\omega/\omega_0)^{-1/2}], & \text{for } \omega/(\omega_0\gamma) \gg 1, \end{cases} \tag{32}$$

and

$$a\lambda_I = \begin{cases} -(\omega/\omega_0)\gamma^{-1/2} + \mathcal{O}[(\omega/\omega_0)^3], & \text{for } \omega/(\omega_0\gamma) \ll 1, \\ -\sqrt{3/8}(\omega/\omega_0)^{1/2} - \mathcal{O}[(\omega/\omega_0)^{-1/2}], & \text{for } \omega/(\omega_0\gamma) \gg 1. \end{cases} \tag{33}$$

The intrinsic frequency

$$\omega_0\gamma = \frac{c^2\rho_0}{\eta} \tag{34}$$

denotes the boundary between the propagating regime, realized for low frequencies $\omega < \omega_0\gamma$ and where compression perturbations lead to propagative waves, characterized by $\lambda_R^{-1} > |\lambda_I^{-1}|$ and a speed of sound $c \sim \omega|\lambda_I^{-1}|$, and the diffusive regime, realized for high frequencies $\omega > \omega_0\gamma$ and where compression perturbations are damped by viscosity effects, characterized by $\lambda_R \sim |\lambda_I| \sim \alpha_R \sim |\alpha_I|$. For water parameters and speed of sound $c \approx 10^3$ m/s, one obtains the intrinsic frequency $\omega_0\gamma \simeq 10^{12}\,\mathrm{s}^{-1}$, *i.e.*, for all realistic frequencies one has $\omega < \omega_0\gamma$ and thus propagating sound waves occur. For higher frequencies, the screening length of compression perturbations is identical to that of shear waves. We note that the crossover frequency $\omega_0\gamma$ can be much lower for systems characterized by a higher compressibility or higher viscosity, *e.g.* liquids close to a critical point or polymers embedded in a solvent. The decay length in the propagative regime, $\lambda_R^{-1} \simeq (\omega_0/\omega)^2 a\gamma^{3/2}$, for water is given by $\lambda_R^{-1} \simeq 10^{15}\ (\omega\,\mathrm{s})^{-2}\,\mathrm{m}$. For frequencies $\omega = 1\,\mathrm{s}^{-1}$ and $\omega = 10^6\,\mathrm{s}^{-1}$, the screening lengths of compression waves are $\lambda_R^{-1} \simeq 10^{15}$ m and $\lambda_R^{-1} \simeq 10^3$ m, respectively, which means that for realistic frequencies this screening length is macroscopic. For non-aqueous systems, on the other hand, the screening length can become microscopic.

3.3 Total Green's function

The total Green's function reflecting both compression and shear effects is constructed by summing eqs. (20) and (26) as

$$\begin{aligned} G_{ij} &= G_{ij}^T + G_{ij}^L \\ &= \frac{1}{4\pi\eta\alpha^2 r^3}\{\delta_{ij}([1+r\alpha+r^2\alpha^2]e^{-r\alpha} - [1+r\lambda]e^{-r\lambda}) \\ &\quad -3\hat{r}_i\hat{r}_j([1+r\alpha+r^2\alpha^2/3]e^{-r\alpha} \\ &\quad -[1+r\lambda+r^2\lambda^2/3]e^{-r\lambda})\}. \end{aligned} \tag{35}$$

According to eqs. (32) and (33), for $\omega < \omega_0\gamma$ the screening length of compression waves λ_R^{-1} is larger than the screening length α_R^{-1} of shear waves and thus an intermediate distance range $\alpha_R^{-1} < r < \lambda_R^{-1}$ exists within which shear waves are screened and decay according to eq. (22) but compression waves are unscreened and described by eq. (27). For small distances, for which $r\lambda \ll 1$ and $r\alpha \ll 1$, the limiting behavior follows from summing up eqs. (21) and (27)

$$G_{ij} \simeq \frac{1}{8\pi\eta r}\left(\delta_{ij}[1+\lambda^2/\alpha^2] + \hat{r}_i\hat{r}_j[1-\lambda^2/\alpha^2]\right). \tag{36}$$

Since the ratio $\lambda^2/\alpha^2 = (4/3+\zeta/\eta+\imath\omega_0\gamma/\omega)^{-1}$ is very small for water, one can neglect this contribution coming from the compression part. In the large-distance regime, for which $r\lambda \gg 1$ and $r\alpha \gg 1$, cancelation of the leading-order terms in eqs. (22) and (28) takes place, by including second-leading-order terms we obtain

$$\begin{aligned} G_{ij} \simeq \frac{1}{4\pi\eta\alpha^2 r^3}&\left\{\delta_{ij}\left([r^2\alpha^2 - r\alpha]e^{-r\alpha} - r\lambda e^{-r\lambda}\right)\right. \\ &\left. +\hat{r}_i\hat{r}_j\left(-[r^2\alpha^2+3r\alpha]e^{-r\alpha} + r^2\lambda^2 e^{-r\lambda}\right)\right\}. \end{aligned} \tag{37}$$

Here an interesting anisotropy of the hydrodynamic response exists: When the force is perpendicular to the connecting vector between source point and field point, one has $\hat{r}_j F_j = 0$ and thus

$$G_{ij}^{\perp} \simeq \frac{1}{4\pi\eta\alpha^2 r^3}\left(r^2\alpha^2 e^{-r\alpha} - r\lambda e^{-r\lambda}\right), \qquad (38)$$

for the parallel contribution one obtains

$$G_{ij}^{\parallel} \simeq \frac{1}{4\pi\eta\alpha^2 r^3}\left(-4r\alpha e^{-r\alpha} + r^2\lambda^2 e^{-r\lambda}\right). \qquad (39)$$

3.4 Surface stress

From the total Green's function for the velocity field one can calculate the Green's function for the stress tensor, denoted by Π_{ijk}, which is defined as

$$\Pi_{ij} = \Pi_{ijk} F_k. \qquad (40)$$

For a more compact notation, we also define the gradient of the Green's function, G_{kij}, via

$$\nabla_k v_i = \nabla_k G_{ij} F_j = G_{kij} F_j. \qquad (41)$$

From the constituting equation, eq. (9), and the solutions given in eqs. (14) and (16), the pressure follows as

$$p = \frac{\rho_0 c^2}{\imath\omega}\nabla_k v_k + p_0, \qquad (42)$$

where p_0 is the constant background pressure. With the definition of the stress tensor, eq. (4), the stress tensor Green's function follows as

$$\Pi_{ijk}/\eta = G_{ijk} + G_{jik} + (\alpha^2/\lambda^2 - 2)G_{llk}\delta_{ij}. \qquad (43)$$

4 Velocity distribution on a plane

The Green's function for a compressible fluid given in eq. (35) can be used to obtain the response function of bodies of different geometries by distributing a source field over the body surface chosen such that the hydrodynamic boundary conditions are satisfied. The simplest case is the response function of an oscillating plane of infinite extent. Here, perpendicular and tangential motions of the plane lead to a clear separation of compression and shear effects and the influence of surface slip is strikingly displayed. The Green's function of an infinite plane is obtained by the surface integral

$$G_{ij}^{pl}(z) = \int_S G_{ij}(x', y', z)\mathrm{d}S(x', y'), \qquad (44)$$

where S indicates the surface. Due to lateral translational invariance, $G_{ij}^{pl}(z)$ only depends on the vertical distance z from the plane and is given by

$$G_{ij}^{pl}(z) = \delta_{jz}\delta_{iz}\frac{\lambda e^{-|z|\lambda}}{2\eta\alpha^2} + (\delta_{jx}\delta_{ix} + \delta_{jy}\delta_{iy})\frac{e^{-|z|\alpha}}{2\eta\alpha}. \qquad (45)$$

In the following we distinguish oscillations perpendicular and parallel to the surface plane. Note that by using the Green's function of an unbounded fluid, we implicitly assume fluid to be present on both sides of the plane. Since the flow is symmetric with respect to the plane, the asymmetric case with fluid on one side only trivially follows from the symmetric solution by multiplying the force by a factor of two.

4.1 Perpendicular motion

From eq. (45), the velocity field caused by an oscillation perpendicular to the surface reads as

$$v_z^{pl,\perp}(z) = F_z^{pl} G_{zz}^{pl}(z) = \frac{F_z^{pl}}{2\eta\alpha^2}\lambda e^{-|z|\lambda}, \qquad (46)$$

where F_z^{pl} is the amplitude of the force acting on the plane per unit area, *i.e.* the pressure. Only motion in the z-direction is generated and exponentially damped away from the surface. Denoting the oscillation amplitude of the surface at the position $z = 0$ as V_z^{pl} and using the kinematic boundary condition,

$$V_z^{pl} = v_z^{pl,\perp}(0) = \frac{F_z^{pl}}{2\eta\alpha^2}\lambda, \qquad (47)$$

we define the perpendicular response function of the plane via

$$\begin{aligned}\mathcal{G}_{\perp}^{pl}(\omega) = \frac{F_z^{pl}}{V_z^{pl}} &= \frac{2\eta\alpha^2}{\lambda} \\ &= \sqrt{2}\rho_0 c\sqrt{\sqrt{1+\left(\frac{4\omega\eta}{3\rho_0 c^2}\right)^2}+1} \\ &\quad -\imath\sqrt{2}\rho_0 c\sqrt{\sqrt{1+\left(\frac{4\omega\eta}{3\rho_0 c^2}\right)^2}-1}. \end{aligned} \qquad (48)$$

Here and in the remainder of the paper, we have set the volume viscosity to zero, *i.e.* $\zeta = 0$. Note that for the case of fluid on one side only the response function is divided by a factor of two. In the low-frequency propagative regime, $\omega < \omega_0\gamma$, the response function shows saturation at a constant value

$$\mathcal{G}_{\perp}^{pl}(\omega) \simeq 2\rho_0 c\left[1 + 2\left(\frac{\omega}{3\omega_0\gamma}\right)^2 - \imath\frac{2\omega}{3\omega_0\gamma}\right], \qquad (49)$$

while in the high-frequency limit, $\omega > \omega_0\gamma$, we find

$$\mathcal{G}_{\perp}^{pl}(\omega) \simeq 2\rho_0 c(1-\imath)\left(\frac{2\omega}{3\omega_0\gamma}\right)^{1/2}. \qquad (50)$$

That the response function saturates at a constant value for $\omega \to 0$ is an artifact of the linearization approximation and will be discussed further in the next section.

4.2 Parallel motion

For shearing motion parallel to the plane, the velocity field is given by

$$v_x^{pl,\parallel}(z) = F_x^{pl} G_{xx}^{pl}(z) = \frac{F_x^{pl}}{2\eta\alpha} e^{-|z|\alpha}. \tag{51}$$

Since no compression occurs, the parameter λ does not appear in this case. We apply the Navier boundary condition at the position of the surface,

$$b \frac{\partial v_x^{pl,\parallel}(z)}{\partial z}\bigg|_{z=0} = v_x^{pl,\parallel}(0) - V_x^{pl}, \tag{52}$$

which relates the fluid shear rate to the tangential velocity component of the fluid at the boundary via the slip length b. For $b = 0$ one has the no-slip boundary condition, finite b corresponds to variable amounts of surface slip. The response function due to the parallel plane oscillations reads

$$\mathcal{G}_\parallel^{pl}(\omega) = \frac{F_x^{pl}}{V_x^{pl}} = \frac{2\eta\alpha}{b\alpha + 1}, \tag{53}$$

or in more explicit form by using eq. (15)

$$\mathcal{G}_\parallel^{pl}(\omega) = 2\eta \frac{b\omega\rho_0/\eta + \sqrt{\omega\rho_0/2\eta} - \imath\sqrt{\omega\rho_0/2\eta}}{b^2\omega\rho_0/\eta + 2b\sqrt{\omega\rho_0/2\eta} + 1}. \tag{54}$$

Note that, in contrast to the perpendicular case, the static response for the parallel geometry is zero, *i.e.* the force needed to tangentially move a plane vanishes in the zero-frequency limit. This is expected since in the static limit $\omega \to 0$ the fluid is comoving with the plane as a whole and the dissipation (and thus the response function) vanishes. That the response for the perpendicular motion saturates at a constant value is due to the neglect of the convective non-linear term in the Navier-Stokes equation and signals a break down of the linearization approximation. In contrast, no convective term is present for the parallel motion case and thus the linear approximation is exact. As for the perpendicular case, if fluid is present on one side of the plane only, the response function is divided by a factor of two and coincides with Stokes' original result [17]. For small frequency the response becomes

$$\mathcal{G}_\parallel^{pl}(\omega) \simeq 2\eta(1 - \imath)\sqrt{\omega\rho_0/2\eta}, \tag{55}$$

which is the same result obtained from the exact expression, eq. (54) in the limit of vanishing slip length, $b = 0$. For high frequencies, $\omega > \omega_b = \eta/(\rho_0 b^2)$, the behavior is distinctly different and we obtain

$$\mathcal{G}_\parallel^{pl}(\omega) \simeq 2\eta \left[b^{-1} - \imath b^{-2}(2\omega\rho_0/\eta)^{-1/2}\right]. \tag{56}$$

Comparison of eqs. (55) and (56) shows that the real part of the response function saturates at a constant value for frequencies higher than ω_b, whereas the imaginary part of the response function exhibits a maximum around the crossover frequency ω_b and goes to zero both for very small and very high frequencies. The crossover frequency ω_b for water and a slip length of $b = 10\,\mathrm{nm}$ as found for hydrophobic materials is of the order of $\omega_b \simeq 10^{10}\,\mathrm{s}^{-1}$. We conclude that for aqueous fluids, very high frequencies and thus advanced experimental techniques are needed to probe the high-frequency slip regime. On the other hand, for fluids with large slip lengths or in confined media, the crossover occurs at lower and thus experimentally more easily accessible frequency scales.

5 Velocity distribution around a sphere

To obtain the fluid velocity around a sphere of radius a, we make a standard singularity ansatz [18]

$$G_{ij}^{sp} = (C_0 + C_2 a^2 \nabla_k \nabla_k) G_{ij}, \tag{57}$$

so that the velocity field follows as $v_i^{sp} = F_j G_{ij}^{sp}$ and F_j is a force source. Both coefficients C_0 and C_2 are functions of the frequency and are determined such that the boundary conditions on the sphere surface are satisfied. Note that the actual force acting on the sphere is not given by the force source but calculated by integration of the surface traction over the sphere surface. Our results for the response function thus correspond to a solid sphere with no fluid inside. In the presence of slip, the boundary condition at the sphere surface splits into the kinematic condition

$$6\pi\eta a \hat{r}_i G_{ij}^{sp} = \hat{r}_j, \tag{58}$$

for $|\mathbf{r}| = a$, which defines the sphere velocity as $V_i^{sp} = F_i/6\pi\eta a$ such that in the steady (zero-frequency) limit, the source force F_i equals the actual force on the sphere. The Navier boundary condition for the tangential stress reads

$$b(\nabla_k G_{ij}^{sp} + \nabla_i G_{kj}^{sp})\hat{r}_k \mathcal{P}_{li} = (G_{ij}^{sp} - \delta_{ij}/6\pi\eta a)\mathcal{P}_{li}, \tag{59}$$

for $|\mathbf{r}| = a$, where the projection operator is defined as $\mathcal{P}_{li} = (\delta_{li} - \hat{r}_l \hat{r}_i)$. The boundary conditions fix both coefficients C_0 and C_2 and the result for G_{ij}^{sp} reads

$$\begin{aligned} G_{ij}^{sp} = & \frac{1}{4\pi\eta\alpha^2 r^3} \\ & \times \left\{ \delta_{ij} \left(E_1[1 + r\alpha + r^2\alpha^2]e^{-r\alpha} - E_2[1 + r\lambda]e^{-r\lambda} \right) \right. \\ & -3\hat{r}_i\hat{r}_j \left(E_1[1 + r\alpha + r^2\alpha^2/3]e^{-r\alpha} \right. \\ & \left.\left. -E_2[1 + r\lambda + r^2\lambda^2/3]e^{-r\lambda} \right) \right\} \end{aligned} \tag{60}$$

with the coefficients

$$E_1 = \frac{2}{3} e^{\tilde{\alpha}} \frac{(1 + 2\tilde{b})(3 + 3\tilde{\lambda} + \tilde{\lambda}^2)}{W}, \tag{61}$$

$$E_2 = \frac{2}{3} e^{\tilde{\lambda}} \frac{(1 + 2\tilde{b})(3 + 3\tilde{\alpha} + \tilde{\alpha}^2) + \tilde{b}\tilde{\alpha}^2(1 + \tilde{\alpha})}{W} \tag{62}$$

and

$$W = (2+2\tilde{\lambda}+\tilde{\lambda}^2)(1+\tilde{b}(3+\tilde{\alpha}))+(1+\tilde{\alpha})(1+2\tilde{b})\tilde{\lambda}^2/\tilde{\alpha}^2. \tag{63}$$

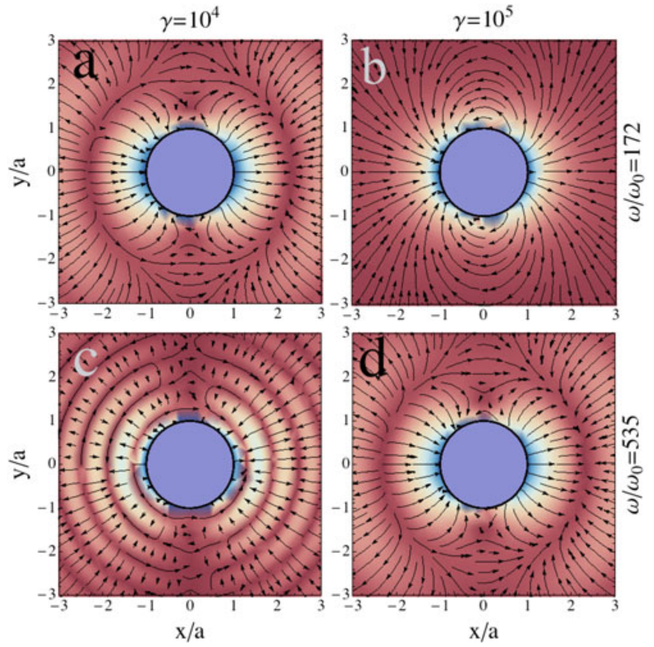

Fig. 1. (Color online) The real part of the velocity field of a sphere, $v_i^{sp} = F_j G_{ij}^{sp}$, oscillating in the x-direction in the xy plane for no slip, $\tilde{b} = 0$. Combinations for two different values of γ and ω/ω_0 are considered. The arrows indicate the direction of the velocity field, while the color denotes the velocity magnitude; the darker (red) the regions are, the smaller the velocity magnitude is. For water, γ values of 10^4 and 10^5 correspond to radii of 10^{-7} m and 10^{-6} m.

Here, we have defined the dimensionless slip length, $\tilde{b} = b/a$, and the dimensionless decay constants $\tilde{\alpha} = a\alpha$ and $\tilde{\lambda} = a\lambda$. In fig. 1 the real part of the velocity vector field $\mathbf{v}^{sp}$ is represented for different parameters in the xy plane with the force applied to the right (x-direction). Within the rows the rescaled frequency ω/ω_0 is constant, within the columns the parameter γ stays constant. The color scale corresponds to the velocity magnitude, while the arrows denote the velocity direction. For all parameter combinations we have $\omega/(\omega_0\gamma) < 1$ and are thus in the propagating wave regime. The discussion is simplified by defining the rescaled propagation wavelength

$$\tilde{\Lambda} = \frac{\Lambda}{a} = \frac{c/a}{\omega/(2\pi)} = \frac{2\pi\gamma^{1/2}\omega_0}{\omega}\,, \tag{64}$$

which follows from eq. (33) in the limit $\omega/(\omega_0\gamma) < 1$. For the parameter combinations on the diagonal we have $\tilde{\Lambda} \simeq 3$, in accord with the wavelength found by visual inspection. In the lower left picture the wavelength is $\tilde{\Lambda} \simeq 1.2$, while in the upper right corner we have $\tilde{\Lambda} \simeq 9$ and thus a full wavelength does not fit in the graph. To connect to aqueous systems, in water $\gamma = 10^4$ and $\gamma = 10^5$ correspond to radii of 10^{-7} m and $a \approx 10^{-6}$ m, respectively. The rescaled frequencies $\omega/\omega_0 = 172$ and $\omega/\omega_0 = 535$ correspond for a radius $a \approx 10^{-6}$ m and water parameters to oscillation frequencies $\omega \simeq 10^8\,\mathrm{s}^{-1}$ and $\omega \simeq 10^9\,\mathrm{s}^{-1}$, respectively. To gain global insight into the flow profiles at an oscillating sphere, we plot in fig. 2 the real parts of the normalized velocity profile for an oscillating force acting along the x-direction; in the upper row we show $v_x^{sp}(x, y = 0)$, *i.e.* the radial flow profile in the direction of the applied force, in the lower row we show $v_x^{sp}(x = 0, y)$, *i.e.* the tangential flow profile. Results are shown for the rescaled wavelengths $\tilde{\Lambda} = 0.2, 1$ and 5 and for frequencies in the propagating and the diffusing wave regimes, *i.e.* for $\omega/(\omega_0\gamma) < 1$ as well as $\omega/(\omega_0\gamma) > 1$, respectively. Indeed, propagating waves are clearly distinguished from diffusing waves for the radial velocity component (upper row), for the tangential flow component (bottom row) the difference is less pronounced. The other interesting observation is that for spheres small compared to the propagation wave length, *i.e.* for $\tilde{\Lambda} = 5$, the amplitude of the velocity field away from the sphere (which in the figure is rescaled by the flow velocity at the sphere surface) is much smaller than for a large sphere. This has to do with destructive interference effects from waves emanating from different regions of the sphere surface.

5.1 Surface stress at a sphere

The expression for the stress-tensor Green's function given in eq. (43) also applies to the spherical case. The derivative of the sphere Green's function reads

$$\begin{aligned} G_{kij}^{sp} = {} & \frac{1}{4\pi\eta r^4\alpha^2} \\ & \times \big\{ \delta_{ij}\hat{r}_k \left(-E_1[3 + 3r\alpha + 2r^2\alpha^2 + r^3\alpha^3]e^{-r\alpha} \right. \\ & \left. + E_2[3 + 3r\lambda + r^2\lambda^2]e^{-r\lambda} \right) \\ & -3(\delta_{ki}\hat{r}_j + \delta_{kj}\hat{r}_i) \left(E_1[1 + r\alpha + r^2\alpha^2/3]e^{-r\alpha} \right. \\ & \left. - E_2[1 + r\lambda + r^2\lambda^2/3]e^{-r\lambda} \right) \\ & +3\hat{r}_k\hat{r}_i\hat{r}_j \left(E_1[5 + 5r\alpha + 2r^2\alpha^2 + r^3\alpha^3/3]e^{-r\alpha} \right. \\ & \left. - E_2[5 + 5r\lambda + 2r^2\lambda^2 + r^3\lambda^3/3]e^{-r\lambda} \right) \big\}\,. \end{aligned} \tag{65}$$

The frequency-dependent hydrodynamic force on a spherical particle follows by projection of the stress tensor on the surface and integration over the sphere surface,

$$F_i^{sp} = -6\pi\eta a V_j^{sp} \int \mathrm{d}^3 r \hat{r}_k \Pi_{kij} \delta(|r| - a), \tag{66}$$

where V_j^{sp} is the frequency-dependent velocity amplitude. The corresponding response function $\mathcal{G}^{sp}(\omega)$ follows as

$$\delta_{ij}\mathcal{G}^{sp}(\omega) = \frac{F_i^{sp}}{V_j^{sp}} = -6\pi\eta a \int \mathrm{d}^3 r \hat{r}_k \Pi_{kij} \delta(|r| - a). \tag{67}$$

In the calculation the identities $\int \mathrm{d}^3 r \delta_{ij} \delta(|r| - a) = 4\pi a^2 \delta_{ij}$ and $\int \mathrm{d}^3 r \hat{r}_i \hat{r}_j \delta(|r| - a) = 4\pi a^2 \delta_{ij}/3$ are used. The response function follows as

$$\mathcal{G}^{sp}(\omega) = \frac{2}{3}E_1 e^{-a\alpha}(1 + a\alpha) + \frac{1}{3}E_2 e^{-a\lambda}(1 + a\lambda) \tag{68}$$

or, in more explicit form, as

$$\begin{aligned} \mathcal{G}^{sp}(\omega) = {} & \frac{4\pi\eta a}{3} W^{-1} \Big[(1 + \tilde{\lambda})(9 + 9\tilde{\alpha} + \tilde{\alpha}^2)(1 + 2\tilde{b}) \\ & + (1 + \tilde{\alpha})(2\tilde{\lambda}^2(1 + 2\tilde{b}) + \tilde{b}\tilde{\alpha}^2(1 + \tilde{\lambda})) \Big]\,, \end{aligned} \tag{69}$$

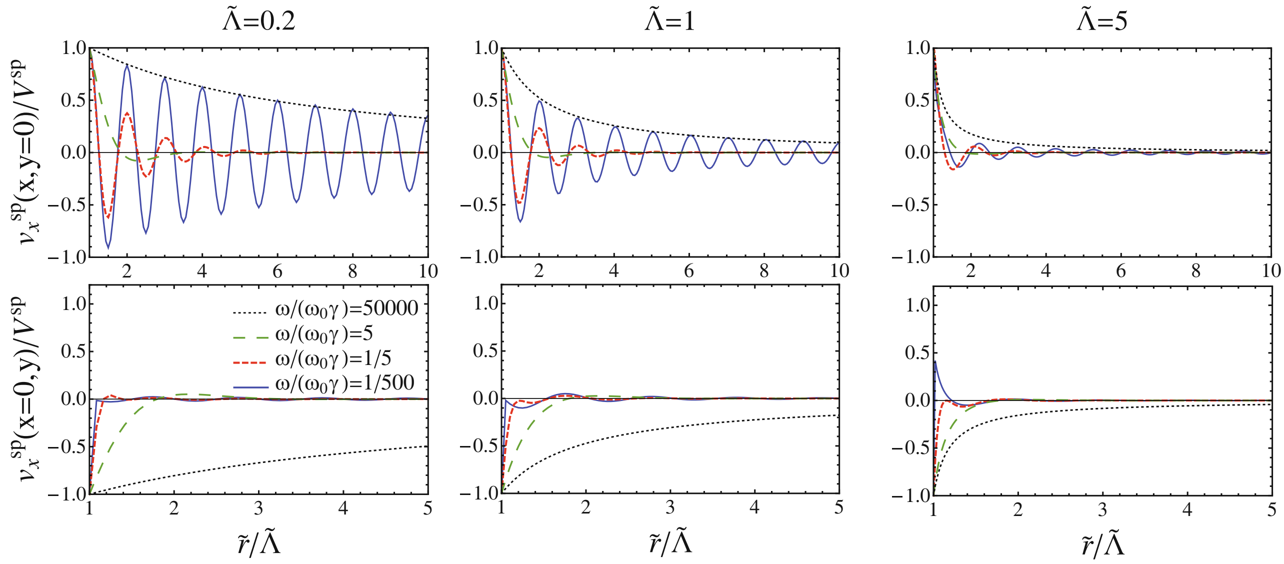

Fig. 2. (Color online) Normalized amplitude of the real part of the velocity field of a sphere for various values of $\omega/(\omega_0\gamma)$ and $\tilde{\Lambda}$ with no-slip boundary condition, $\tilde{b}=0$. The upper row shows $v_x^{sp}(x,y=0)$, *i.e.* the radial flow profile in the direction of the applied force; the lower row shows $v_x^{sp}(x=0,y)$, *i.e.* the tangential flow profile. The oscillating force acts along the x-direction.

where W is given by eq. (63). To investigate the asymptotic behavior of eq. (69), we define real and imaginary parts according to

$$\mathcal{G}^{sp}(\omega) = \mathcal{G}'^{sp}(\omega) + \imath\mathcal{G}''^{sp}(\omega). \tag{70}$$

For the real part we obtain the asymptotic behavior

$$\frac{\mathcal{G}'^{sp}(\omega)}{6\pi\eta a} \simeq \begin{cases} \text{for } \omega \to 0 \quad \frac{1+2\tilde{b}}{1+3\tilde{b}} + \frac{(1+2\tilde{b})^2\sqrt{\omega/\omega_0}}{\sqrt{2}(1+3\tilde{b})^2} + \mathcal{O}[\omega/\omega_0], \\ \text{for } \omega \to \infty \\ \quad \frac{2}{9}\sqrt{\frac{2}{3}}\sqrt{\omega/\omega_0} + \frac{4(3+4\tilde{b})}{27\tilde{b}} + \mathcal{O}[(\sqrt{\omega/\omega_0})^{-1}] \end{cases} \tag{71}$$

and for the imaginary part we obtain

$$\frac{\mathcal{G}''^{sp}(\omega)}{6\pi\eta a} \simeq \begin{cases} \text{for } \omega \to 0 \\ \quad -\frac{(1+2\tilde{b})^2\sqrt{\omega/\omega_0}}{\sqrt{2}(1+3\tilde{b})^2} \\ \quad +\frac{\omega/\omega_0\left(9-2\gamma+63\tilde{b}+18\tilde{b}^2(8+\gamma)+18\tilde{b}^3(6+\gamma)\right)}{18(1+3\tilde{b})^3\gamma} \\ \quad +\mathcal{O}[(\omega/\omega_0)^{3/2}], \\ \text{for } \omega \to \infty \\ \quad -\frac{2}{9}\sqrt{\frac{2}{3}}\sqrt{\omega/\omega_0} \\ \quad +\frac{-24+32\left(-3+\sqrt{3}\right)\tilde{b}+\left(-96+\sqrt{3}(64+3\gamma)\right)\tilde{b}^2}{54\sqrt{2}\sqrt{\omega/\omega_0}\,\tilde{b}^2} \\ \quad +\mathcal{O}[(\omega/\omega_0)^{-1}]. \end{cases} \tag{72}$$

As $\omega \to 0$, the real part of the response function goes to $6\pi\eta a$ for $\tilde{b} \to 0$ and $4\pi\eta a$ for $\tilde{b} \to \infty$, the standard steady-state results [17]. The compressibility effects (which are parameterized by the parameter γ) are rather mild and only show up in higher-order corrections.

As the normalized slip length $\tilde{b}$ goes to zero, which corresponds to the no-slip boundary condition, eq. (69) turns into

$$\mathcal{G}^{sp}(\omega) = \frac{4\pi\eta a}{3}\frac{(1+\tilde{\lambda})(9+9\tilde{\alpha}+\tilde{\alpha}^2)+2\tilde{\lambda}^2(1+\tilde{\alpha})}{2(1+\tilde{\lambda})+(1+\tilde{\alpha}+\tilde{\alpha}^2)\tilde{\lambda}^2/\tilde{\alpha}^2}, \tag{73}$$

which is consistent with previous results obtained by Bedeaux and Muzar [12]. In the incompressible limit, when $\tilde{\lambda} \to 0$, eq. (73) crosses over to $\mathcal{G}^{sp}(\omega) = 6\pi\eta a(1 + a\alpha + a^2\alpha^2/9)$, the well-known Stokes result [17].

In the limit of $b \to \infty$, the perfect slip case as realized for bubbles, eq. (69), reads

$$\mathcal{G}^{sp}(\omega) = \frac{4\pi\eta a}{3} \times \frac{(1+\tilde{\lambda})(18+18\tilde{\alpha}+3\tilde{\alpha}^2+\tilde{\alpha}^3)+4(1+\tilde{\alpha})\tilde{\lambda}^2}{(2+2\tilde{\lambda}+\tilde{\lambda}^2)(3+\tilde{\alpha})+2(1+\tilde{\alpha})\tilde{\lambda}^2/\tilde{\alpha}^2}. \tag{74}$$

Again, taking the incompressible limit, corresponding to $\tilde{\lambda} \to 0$, eq. (74) reduces to

$$\mathcal{G}^{sp}(\omega) = 6\pi\eta a\frac{(2+2\tilde{\alpha}+\tilde{\alpha}^2/3+\tilde{\alpha}^3/9)}{(3+\tilde{\alpha})}, \tag{75}$$

which is Stokes' incompressible result for perfect slip boundary conditions.

Figure 3 illustrates the effect of compressibility for zero slip, $\tilde{b} = 0$, corresponding to the result given in eq. (73). The compressibility is tuned by changing γ from 10^2 (which is indistinguishable from the $\gamma = 0$ limit) to ∞, the higher γ, the more incompressible the liquid. What is remarkable is that both asymptotic limits, $\gamma = 0$ and

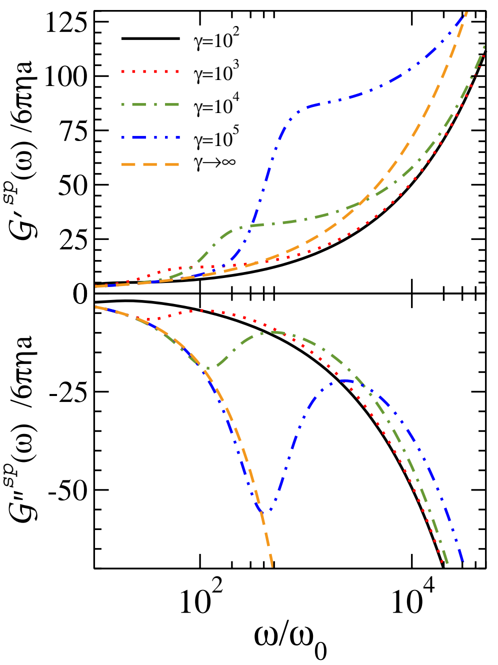

Fig. 3. (Color online) Real and imaginary parts of the rescaled response function of a sphere, $\mathcal{G}^{sp}(\omega) = \mathcal{G}'^{sp}(\omega) + \imath\mathcal{G}''^{sp}(\omega)$, for no-slip boundary condition, $\tilde{b} = 0$, given by eq. (73), as a function of the rescaled frequency ω/ω_0 for different values of γ. The volume viscosity ζ is set to 0. Note that for the given scale, curves for $\gamma = 10^2$ and $\gamma \to 0$ are indistinguishable.

$\gamma = \infty$, corresponding to a fluid of vanishing and infinite sound velocity, respectively, are finite and well behaved, in agreement with the asymptotic expansion in eqs. (71) and (72). Furthermore, the dependence of the response function on γ is non-monotonic.

In fig. 4 the response function is shown for five different γ values, $\gamma = 10^{-3}$, 10^{-1}, 10^2, 10^5 and 10^{10}, which correspond to sphere radii of $a = 10^{-12}$ m, 10^{-10} m, 10^{-8} m, 10^{-6} m and 10^{-4} m in water, respectively. These graphs reveal a pronounced dependence on the slip length, particularly for high frequencies. From the plots a double resonance behavior of the imaginary part is discerned. A sharp minimum is observed for high γ values, while for $\gamma \ll 1$, the minimum is less pronounced and the maximum is more visible. These extrema are defined by the equation

$$\left.\frac{\partial \mathcal{G}''^{sp}(\omega)}{\partial \omega}\right|_{\omega^*} = 0. \tag{76}$$

Based on asymptotic analysis, the minimum $\omega^*_{\rm min}$ obeys the scaling laws

$$\omega^*_{\rm min} \simeq \begin{cases} \text{for } \gamma \to 0 \\ \quad \frac{1}{2}\omega_0\gamma^2 - \frac{23}{18}\omega_0\gamma^3 + \mathcal{O}(\gamma^4), \\ \text{for } \gamma \to \infty \\ \quad \sqrt{2}\omega_0\gamma^{1/2} - 2.15822\,\omega_0\gamma^{1/4} + \mathcal{O}(1) \approx c/a, \end{cases} \tag{77}$$

and the maximum scales as

$$\omega^*_{\rm max} \simeq \begin{cases} \text{for } \gamma \to 0: \\ \quad \text{for } b = 0 \\ \qquad \frac{6}{11}\,\omega_0\gamma - 0.54628\,\omega_0\gamma^{3/2} + \mathcal{O}(\gamma^2) \\ \qquad\qquad \approx c^2\rho_0/\eta, \\ \quad \text{for } b \neq 0 \\ \qquad \frac{6+18\tilde{b}}{11+30\tilde{b}}\,\omega_0\gamma + \mathcal{O}(\gamma^{3/2}), \\ \text{for } \gamma \to \infty: \\ \quad \text{for } b = 0 \\ \qquad 2^{1/3}\omega_0\gamma^{2/3} - \frac{20}{9}\omega_0\gamma^{1/2} + \mathcal{O}(\gamma^{1/3}), \\ \quad \text{for } b \neq 0 \\ \qquad \sqrt{3/2}\,\omega_0\gamma^{3/4} + \mathcal{O}(\gamma^{1/4}). \end{cases} \tag{78}$$

In fig. 5, $\omega^*_{\rm min}/\omega_0$ and $\omega^*_{\rm max}/\omega_0$ as determined numerically from the solution of eq. (76), dotted and broken lines, are compared to the asymptotic scaling laws (solid straight lines). The most pronounced features in fig. 4 are obtained for $\omega^*_{\rm min}$ for large γ and for $\omega^*_{\rm max}$ for small γ, for which we now advance some simple scaling ideas. In fact, $\omega^*_{\rm min}$ for large γ equals $\omega^*_{\rm min} \sim \omega_0\gamma^{1/2} \sim c/a$, which is the inverse time a propagating compression wave needs to travel a distance corresponding to the sphere size a. This resonance can therefore be thought of as due to interference between waves emanating from different parts of the sphere. As γ decreases and reaches unity, this scaling law hits the boundary between the diffusive and propagative regimes, which scales as $\omega \sim \omega_0\gamma$, and thus the above scaling description of the resonance becomes invalid. The diffusive regime is indicated in fig. 5 by a dark shading. In fact, in the limit of small γ a maximum shows up right at the boundary between the diffusive and propagative regime with the scaling $\omega^*_{\rm max} \sim \omega_0\gamma$. This resonance-like feature is caused by interference due to the linear addition of compression and shear effects, and related to the fact that compression waves are marginally propagative.

6 Velocity distribution around a cylinder

The Green's function approach is now applied to cylinders. This problem has been studied in the past for incompressible fluids by several authors [23,24]. We consider a cylinder as illustrated in fig. 6 of radius a aligned along the z-direction and treat oscillations parallel and perpendicular to the long axis.

We first derive the Green's function of a line source. To that end, we integrate the Green's function given in eq. (35) over z as

$$G^{\rm line}_{ij}(\sigma) = \int_{-\infty}^{+\infty} {\rm d}z G_{ij}(x, y, z), \tag{79}$$

where $\sigma = x^2 + y^2$. After some algebra detailed in appendix A.1, the line Green's function can be expressed in terms of Bessel functions and separated into shear (transverse) and compression (longitudinal) contributions. The result is

$$G^{\rm line}_{ij} = G^{{\rm line},T}_{ij} + G^{{\rm line},L}_{ij} \tag{80}$$

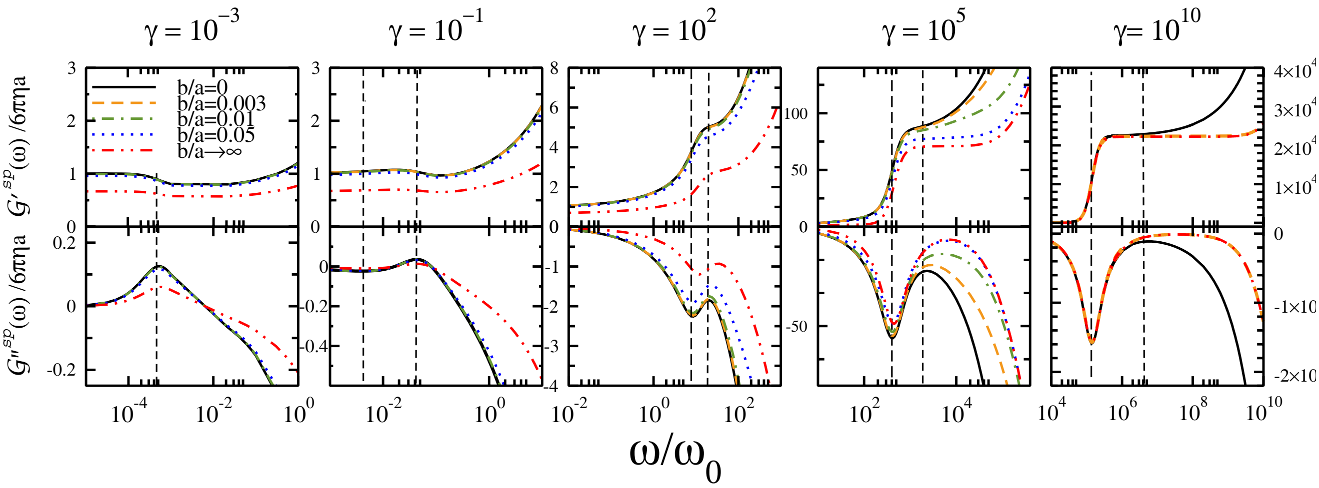

Fig. 4. (Color online) Real and imaginary parts of the rescaled response function of a sphere, $\mathcal{G}^{sp}(\omega) = \mathcal{G}'^{sp}(\omega) + \imath\mathcal{G}''^{sp}(\omega)$, given by eq. (69), as a function of the rescaled frequency, ω/ω_0 for various normalized slip lengths, $\tilde{b}$ and different values of γ. For water, γ values of 10^{-3}, $10^{-1}10^{2}$, 10^{5} and 10^{10} correspond to radii $a = 10^{-12}\,$m, $10^{-10}\,$m, $10^{-8}\,$m, $10^{-6}\,$m and $10^{-4}\,$m, respectively. The vertical dashed lines denote the resonant frequency for vanishing slip length, $\tilde{b} = 0$. The volume viscosity ζ is set to 0.

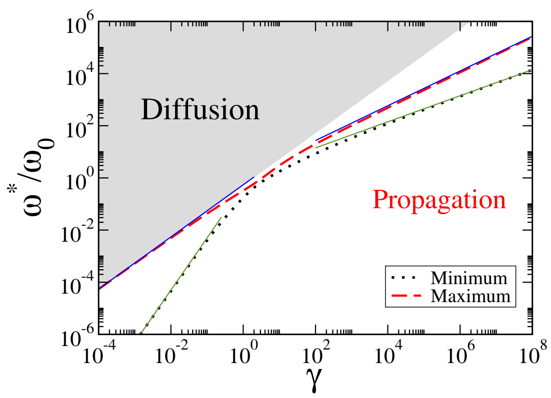

Fig. 5. (Color online) Rescaled resonance frequencies ω^*/ω_0 of a sphere for vanishing slip length, $\tilde{b} = 0$, as a function of γ. We distinguish a local maximum of the imaginary response function $\mathcal{G}''^{sp}(\omega)$ (broken line) from the local minimum (dotted line). Asymptotic laws given by eqs. (77) and (78) are denoted by solid lines. The extrema are indicated by the vertical dashed lines in fig. 4. The grey area denotes the diffusive regime, where compression perturbations are overdamped, while in the white area compression perturbations give rise to propagating waves.

(see appendix A.1 for details). In the following sections, we explicitly calculate the Green's functions for parallel and perpendicular motions.

6.1 Perpendicular motion

We first consider motion perpendicular to the long axis, *i.e.* the Cartesian indices i and j take the values x and y only. Similar to the singularity ansatz for the sphere, eq. (57), we write the Green's function for the cylinder

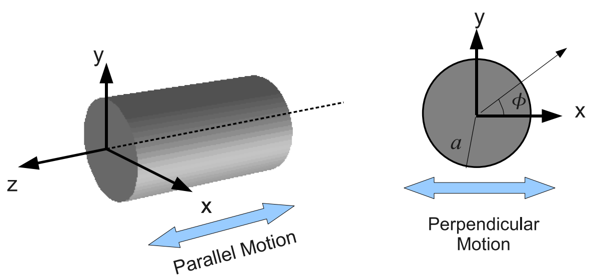

Fig. 6. Illustration of a cylinder with radius a in Cartesian coordinates. The parallel motion is defined along the z-direction.

with finite radius as

$$\begin{aligned} G_{ij}^{\mathrm{cyl},\perp} &= D_0 G_{ij}^{\mathrm{line}} + D_2 a^2 \nabla^2 G_{ij}^{\mathrm{line}}, \\ &= E_1^{\mathrm{cyl}} G_{ij}^{\mathrm{line},T} + E_2^{\mathrm{cyl}} G_{ij}^{\mathrm{line},L}, \end{aligned} \tag{81}$$

see appendix A.1 for details. The coefficients E_1^{cyl} and E_2^{cyl} are frequency dependent and determined by the boundary conditions. The normal component of the velocity field at the cylinder surface satisfies

$$F_k \hat{r}_i G_{ij}^{\mathrm{cyl},\perp} = V_k^{\mathrm{cyl}} \hat{r}_j, \tag{82}$$

for $|\boldsymbol{\sigma}| = a$, where V_k^{cyl} is the velocity of the cylinder in perpendicular motion and F_k is the source with units of force per unit length. The Navier boundary condition for the tangential velocity component reads

$$b(\nabla_k G_{ij}^{\mathrm{cyl},\perp} + \nabla_i G_{kj}^{\mathrm{cyl},\perp})\hat{r}_k \mathcal{P}_{li} = (G_{ij}^{\mathrm{cyl},\perp} - \delta_{ij} F_k / V_k^{\mathrm{cyl}})\mathcal{P}_{li} \tag{83}$$

and holds for $|\boldsymbol{\sigma}| = a$, where the projection operator is defined as $\mathcal{P}_{li} = (\delta_{li} - \hat{r}_l \hat{r}_i)$. Applying these boundary

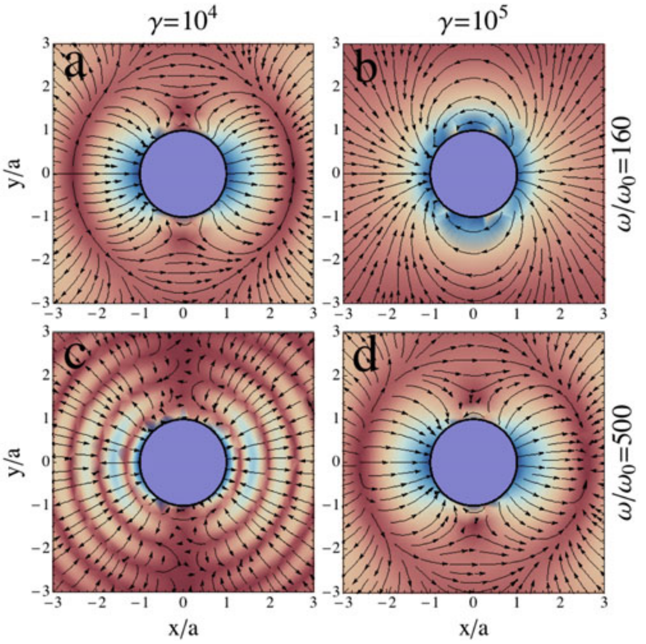

Fig. 7. (Color online) The real part of the velocity field of a perpendicularly oscillating cylinder, $v_i^{\mathrm{cyl},\perp} = F_j G_{ij}^{\mathrm{cyl},\perp}$, in the xy plane for no slip, $\tilde{b} = 0$. The oscillation is along the x-direction. The axes are normalized by the cylinder radius, and the arrows indicate the direction of the velocity vector. The darker (red) the regions are, the smaller the velocity magnitude is. Combinations for two different values of γ and ω/ω_0 are considered. For water, γ values of 10^4 and 10^5 correspond to radii of 10^{-7} m and 10^{-6} m.

conditions on $G_{ij}^{\mathrm{cyl},\perp}$ determines the coefficients as

$$E_1^{\mathrm{cyl}} = -\frac{2\pi\eta\alpha^2}{F_i/V_i^{\mathrm{cyl}}}\frac{N_1+N_2}{N_2M_1-N_1M_2},$$

$$E_2^{\mathrm{cyl}} = \frac{2\pi\eta\alpha^2}{F_i/V_i^{\mathrm{cyl}}}\frac{M_1+M_2}{N_2M_1-N_1M_2}, \tag{84}$$

where the coefficients N_i and M_i can be expressed in terms of Bessel functions as

$$\begin{aligned} M_1 &= -2(\alpha/a)\tilde{b}[2K_1(\alpha a)+\alpha a K_0(\alpha a)] - \tilde{b}\alpha^3 a K_1(\alpha a) \\ &\quad -(\alpha/a)[K_1(\alpha a)+\alpha a K_0(\alpha a)], \\ M_2 &= -(\alpha/a)K_1(\alpha a), \\ N_1 &= 2(\lambda/a)\tilde{b}[2K_1(\lambda a)+\lambda a K_0(\lambda a)] + (\lambda/a)K_1(\lambda a), \\ N_2 &= (\lambda/a)[K_1(\lambda a)+\lambda a K_0(\lambda a)]. \end{aligned} \tag{85}$$

In fig. 7, we show the real part of the velocity field, $v_i^{\mathrm{cyl},\perp} = F_j G_{ij}^{\mathrm{cyl},\perp}$, for various fluid parameters. In the columns γ is constant while in the rows ω/ω_0 is constant. The color scale is a measure of the magnitude of the velocity, in the dark (red) regions the velocity is zero. For water γ values 10^4 and 10^5 correspond to radii of 10^{-7} m and $a \approx 10^{-6}$ m, respectively. Since with the parameters chosen, all four systems belong to the propagative regime, the wavelengths discernable in the plots correspond to the predictions of eq. (64).

In fig. 8, the real part of the flow field of a cylinder in perpendicular motion is shown for various normalized wavelengths $\tilde{\Lambda} = 0.2, 1$ and 5, as in the sphere problem. For each $\tilde{\Lambda}$ value, velocity fields for different $\omega/(\omega_0\gamma)$ values 500, 5, 1/5 and 1/500 are shown. The upper row shows $v_x^{\mathrm{cyl},\perp}(x, y=0)$, *i.e.* the radial flow profile in the direction of the oscillation, the lower row shows $v_x^{\mathrm{cyl},\perp}(x=0, y)$, *i.e.* the tangential flow profile. For $\omega/(\omega_0\gamma) = 1/500$, waves are clearly seen (blue solid line), however, as $\omega/(\omega_0\gamma)$ increases, the number of waves observed goes down. As the rescaled wavelength, $\tilde{\Lambda} = \Lambda/a$, increases, the amplitude of the velocity in the far field decreases because of interference effects, however, this effect is smaller than for the spherical case shown in fig. 2.

6.1.1 Surface stress at a cylinder due to perpendicular motion

The stress Green's function defined in eqs. (41) and (43) also holds for the cylindrical geometry. The force acting on the cylinder per unit length is calculated by the integration of the traction force over the perimeter of the cylinder

$$F_i^{\mathrm{cyl}} = -F_j \int \mathrm{d}^2 r \hat{r}_k \Pi_{kij}\delta(|r|-a), \tag{86}$$

where F_j is the source in the units of force per length. The cylindrical response function is defined as

$$\delta_{ij}\mathcal{G}_\perp^{\mathrm{cyl}}(\omega) = \frac{F_i^{\mathrm{cyl}}}{V_j^{\mathrm{cyl}}} = -\frac{F_l}{V_j^{\mathrm{cyl}}}\int \mathrm{d}^2 r \hat{r}_k \Pi_{kil}\delta(|r|-a), \tag{87}$$

where we make use of the identities $\int \mathrm{d}^2 r \delta_{ij}\delta(|r|-a) = 2\pi a\delta_{ij}$ and $\int \mathrm{d}^2 r \hat{r}_i\hat{r}_j\delta(|r|-a) = \pi a\delta_{ij}$. The final result for the cylindrical response function reads

$$\delta_{ij}\mathcal{G}_\perp^{\mathrm{cyl}}(\omega) = \frac{F_i/V_j^{\mathrm{cyl}}}{2}\left(E_1^{\mathrm{cyl}}\tilde{\alpha}K_1(\tilde{\alpha}) + E_2^{\mathrm{cyl}}\tilde{\lambda}K_1(\tilde{\lambda})\right), \tag{88}$$

where $\tilde{\alpha} = a\alpha$ and $\tilde{\lambda} = a\lambda$. Note that the prefactor F_i/V_j^{cyl} cancels the factors V_j^{cyl}/F_i in the expressions for E_1^{cyl} and E_2^{cyl} in eq. (84). In the incompressible limit, $\lambda \to 0$, and for the no-slip condition, $b = 0$, the above equation crosses over to the known non-steady solution for the incompressible flow field at a cylinder [23], which is explicitly demonstrated in appendix A.4. The asymptotic behavior of $\mathcal{G}_\perp^{\mathrm{cyl}}$ is obtained by asymptotic analysis of the modified Bessel function such as $K_0(x) \simeq -\ln x$ and $K_1(x) \simeq 1/x$ for $\omega \to 0$ and $K_n(x) \simeq e^{-x}/\sqrt{x}$ for $\omega \to \infty$. Using again the separation into real and imaginary parts as in eq. (70),

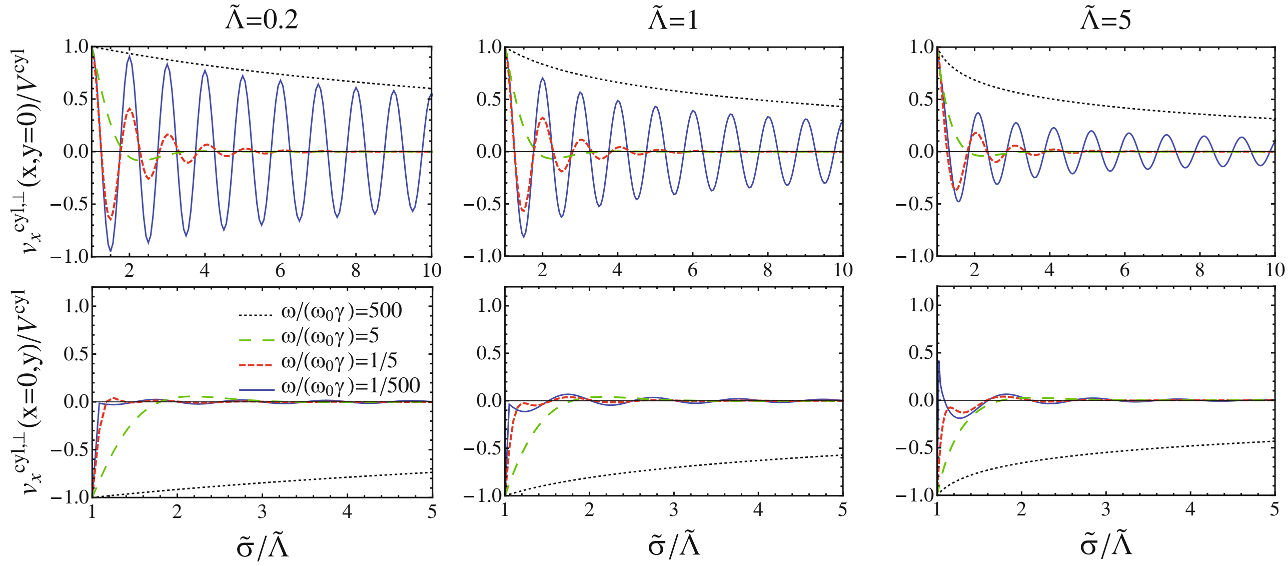

Fig. 8. (Color online) The normalized amplitude of the real part of the velocity field generated by a perpendicularly oscillating cylinder, for various values of $\omega/(\omega_0\gamma)$ and $\tilde{\Lambda}$ with no-slip condition, $\tilde{b}=0$. The upper row shows $v_x(x,y=0)$, *i.e.* the radial flow profile in the direction of the applied force; the lower row shows $v_x(x=0,y)$, *i.e.* the tangential flow profile. The oscillating force acts along the x-direction and the distance is normalized by the wavelength given by eq. (64).

the asymptotic behavior follows as

$$\frac{\mathcal{G}_\perp^{\prime\mathrm{cyl}}(\omega)}{\pi\eta} \simeq \begin{cases} \text{for } \omega\to 0 \\ -\frac{8}{(1+2\tilde{b})^2\ln(\omega/\omega_0)}+\frac{16\tilde{b}}{[(1+2\tilde{b})\ln(\omega/\omega_0)]^2} \\ +\mathcal{O}(\omega/\omega_0), \\ \text{for } \omega\to\infty \\ \sqrt{\frac{2}{3}}\sqrt{\omega/\omega_0}+\frac{3+4b}{3b}+\mathcal{O}[(\sqrt{\omega/\omega_0})^{-1}]. \end{cases} \tag{89}$$

$$\frac{\mathcal{G}_\perp^{\prime\prime\mathrm{cyl}}(\omega)}{\pi\eta} \simeq \begin{cases} \text{for } \omega\to 0 \\ -\frac{4\pi}{[(1+2\tilde{b})\ln(\omega/\omega_0)]^2}+\mathcal{O}(\omega/\omega_0), \\ \text{for } \omega\to\infty \\ -\sqrt{\frac{2}{3}}\sqrt{\omega/\omega_0}+\mathcal{O}[(\sqrt{\omega/\omega_0})^{-1}]. \end{cases} \tag{90}$$

In contrast to the spherical case, the steady-state solution obtained in the limit $\omega\to 0$ goes to zero logarithmically, whereas at high frequency a divergence as $\omega^{1/2}$ is found, identical to the sphere case. Plots of $\mathcal{G}_\perp^{\mathrm{cyl}}(\omega)$ are given in figs. 9 and 10 for $\tilde{b}=0$ and $\tilde{b}\neq 0$, respectively. Figure 9 shows the effects of varying the compressibility parameter γ, fig. 10 demonstrates the effect of varying the slip length $\tilde{b}$ for given γ. For water, the γ values considered, $\gamma=10^{-3}$, 10^{-1}, 10^2, 10^6 and 10^{10}, correspond to radii $a=10^{-12}$ m, 10^{-10} m, 10^{-8} m, 10^{-6} m and 10^{-4} m, respectively.

The effect of surface slip is illustrated in fig. 11 which shows $\mathcal{G}_\perp^{\prime\mathrm{cyl}}(\omega)$ *versus* $\tilde{b}=b/a$ for fixed $\gamma=10^2$. Each curve corresponds to a fixed ω/ω_0 value between 10^{-1} and 10^3 from bottom (red) to top (green), respectively. At low frequency, $\mathcal{G}'^{\mathrm{cyl}}(\omega)$ changes only little with varying slip length (curves at the bottom), but for higher frequency the slip length has a considerable effect on $\mathcal{G}'^{\mathrm{cyl}}(\omega)$ (curves at the top).

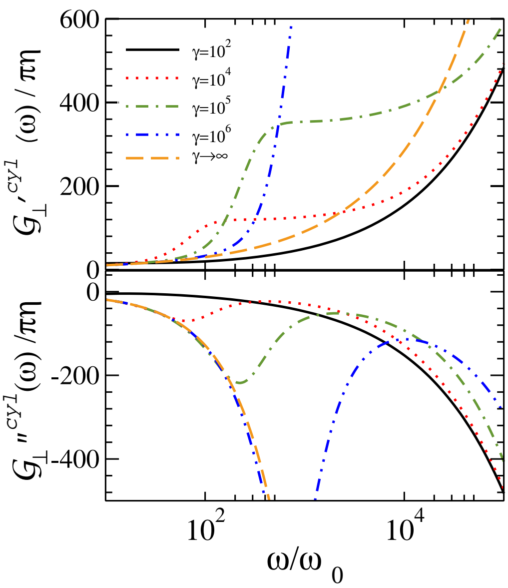

Fig. 9. (Color online) Real and imaginary parts of the response function of a cylinder for perpendicular motion given by eq. (88) with no-slip boundary condition, $\tilde{b}=0$, as a function of the compressibility parameter γ. The volume viscosity ζ is set to 0. Note that, for the given scale, the curves for $\gamma=10^2$ and $\gamma\to 0$ are indistinguishable.

As seen from the response functions in figs. 9 and 10, also for the cylindrical geometry a resonant behavior is obtained. The asymptotic scaling of the resonance where the imaginary response shows a minimum obeys the asymp-

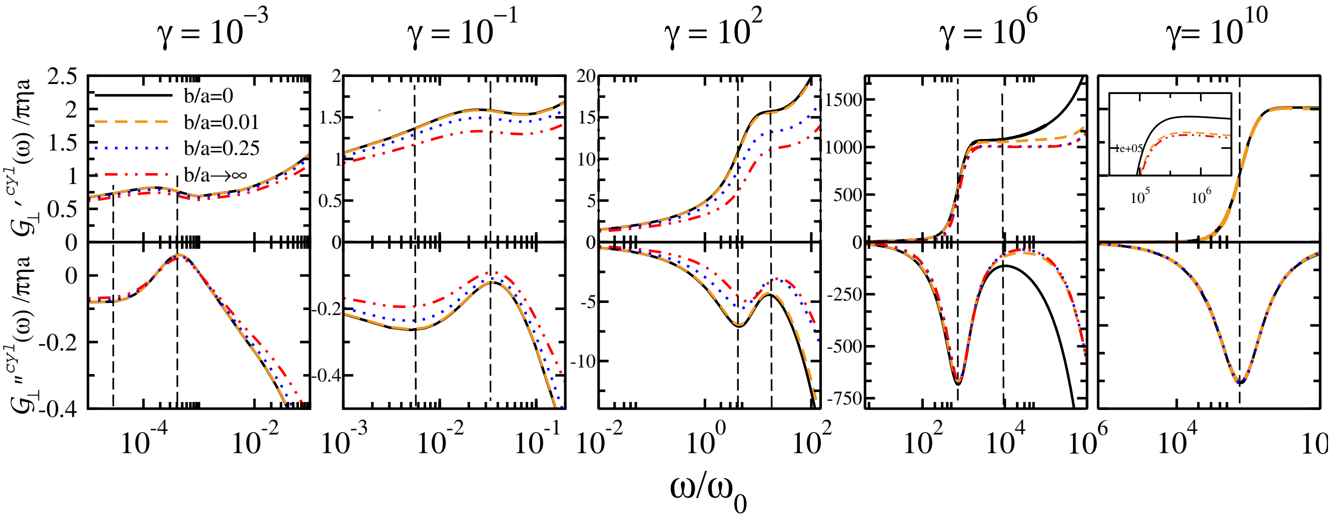

Fig. 10. (Color online) Real and imaginary parts of the rescaled response function of a cylinder in perpendicular motion given by eq. (88) as a function of the rescaled frequency ω/ω_0 for various $\tilde{b}$ and γ values. For water, γ values of 10^{-3}, 10^{-1}, 10^{2}, 10^{6} and 10^{10} correspond to radii $a = 10^{-12}$ m, 10^{-10} m, 10^{-8} m, 10^{-6} m and 10^{-4} m, respectively. The vertical dashed lines denote the resonance frequencies for vanishing slip length, $\tilde{b} = 0$. The volume viscosity ζ is set to 0.

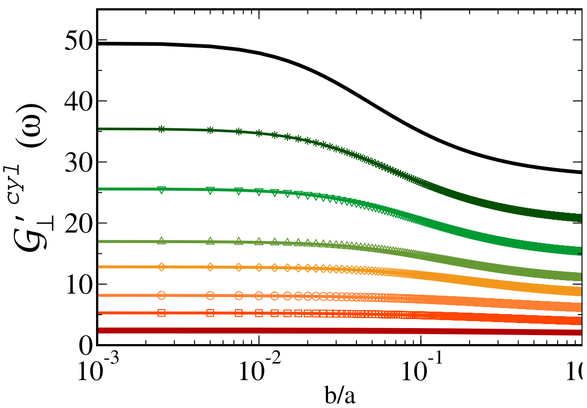

Fig. 11. (Color online) Real part of the response function $\mathcal{G}'^{\rm cyl}_{\perp}(\omega)$ given by eq. (88) for a cylinder oscillating perpendicular to its long axis as a function of the normalized slip length, $\tilde{b} = b/a$. The curves are for constant ω/ω_0 values of 10^{-1}, 1, 5, 50, 100, 250, 500 and 10^3 from bottom to top, respectively. The compressibility constant is $\gamma = 10^2$. The volume viscosity ζ is set to 0.

totic scaling laws

$$\omega^*_{\rm min} \simeq \begin{cases} \text{for } \gamma \to 0 \\ \quad -\omega_0 \gamma \ln \gamma + \mathcal{O}(\gamma^2), \\ \text{for } \gamma \to \infty \\ \quad 0.77129\, \omega_0 \gamma^{1/2} + \mathcal{O}(\gamma^{1/4}) \approx c/a, \end{cases} \tag{91}$$

and the maximum scales as

$$\omega^*_{\rm max} \simeq \begin{cases} \text{for } \gamma \to 0 \\ \quad 4.31252\, \omega_0 \gamma + \mathcal{O}(\gamma^{3/2}) \approx c^2 \rho_0/\eta, \\ \text{for } \gamma \to \infty \\ \quad 2^{1/3} \omega_0 \gamma^{2/3} + \mathcal{O}(\gamma^{1/2}). \end{cases} \tag{92}$$

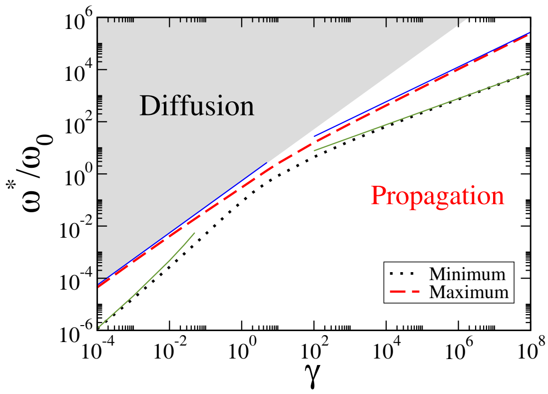

Fig. 12. (Color online) Rescaled resonance frequencies ω^*/ω_0 of a cylinder in perpendicular motion for vanishing slip length, $\tilde{b} = 0$, as a function of γ. We distinguish a local maximum of the imaginary response function $\mathcal{G}''^{\rm cyl}_{\perp}(\omega)$ (broken line) from the local minimum (dotted line). Solid lines are scaling laws given in eqs. (91) and (92). The extrema are indicated by the vertical dashed lines in fig. 10. The grey area denotes the diffusive regime, where compression perturbations are overdamped, while in the white area compression perturbations give rise to propagating waves.

These function are displayed in fig. 12. Except the term involving the logarithmic correction for small γ, the result is identical to the sphere case.

6.2 Parallel motion

For parallel oscillations of the cylinder, the velocity field can be calculated directly from the line Green's function given in eq. (80). The cylinder Green's function reads

$$G_{zz}^{\mathrm{cyl},\parallel} = C_0 G_{zz}^{\mathrm{line}}, \tag{93}$$

where the coefficient C_0 is determined by the boundary condition at the cylinder surface. Using results given in appendix A.1, the line Green function for the parallel motion can be written as

$$G_{zz}^{\mathrm{line}}(\sigma) = \frac{1}{2\pi\eta} K_0(\alpha\sigma) \tag{94}$$

and is independent of the compressibility parameter γ. Similar to a tangentially moved plane, the parallel motion of a cylinder generates only shear. The Navier boundary condition at $|\boldsymbol{\sigma}| = a$ reads

$$b\frac{\partial v_z^{\mathrm{cyl},\parallel}}{\partial\sigma} = (v_z^{\mathrm{cyl},\parallel} - V_z^{\mathrm{cyl}}), \tag{95}$$

where V_z^{cyl} is the velocity of the cylinder, the fluid velocity field is $v_z^{\mathrm{cyl},\parallel} = F_z G_{zz}^{\mathrm{cyl},\parallel}$, and F_z is the source in units of a force per length. After some algebra and with the help of recursion relations introduced in appendix A.1, we obtain

$$C_0 = \frac{2\pi\eta}{F_z/V_z^{\mathrm{cyl}}[b\alpha K_1(\alpha a) + K_0(\alpha a)]} \tag{96}$$

and thus, according to eq. (93),

$$G_{zz}^{\mathrm{cyl},\parallel}(\sigma) = \frac{K_0(\alpha\sigma)}{F_z/V_z^{\mathrm{cyl}}[b\alpha K_1(\alpha a) + K_0(\alpha a)]}. \tag{97}$$

6.2.1 Surface stress at cylinder due to parallel motion

The force on the cylinder per unit length is calculated by integrating the surface traction over the perimeter of the cylinder

$$\begin{aligned} F_z^{\mathrm{cyl},\parallel} &= -\int_0^{2\pi}\int_0^a \mathrm{d}\theta\sigma\mathrm{d}\sigma \frac{\partial v_z^{\mathrm{cyl},\parallel}(\sigma)}{\partial\sigma}\delta(|\sigma| - a) \\ &= F_z C_0 \alpha a K_1(\alpha a). \end{aligned} \tag{98}$$

The response function due the parallel motion of the cylinder follows as

$$\begin{aligned} \mathcal{G}_\parallel^{\mathrm{cyl}}(\omega) &= \frac{F_z^{\mathrm{cyl},\parallel}}{V_z^{\mathrm{cyl}}} \\ &= 2\pi\eta \frac{\tilde{\alpha} K_1(\tilde{\alpha})}{\tilde{b}\tilde{\alpha} K_1(\tilde{\alpha}) + K_0(\tilde{\alpha})}. \end{aligned} \tag{99}$$

In the limit of infinite radius, $a \to \infty$, this response function turns into the response function of a tangentially oscillating plane given in eq. (53), as expected and demonstrated in appendix A.3. In fig. 13, the above response function is illustrated for various slip lengths. The asymptotic behavior of eq. (99) in the limit $\omega \to 0$ reads

$$\mathcal{G}_\parallel^{\mathrm{cyl}}(\omega) \simeq 2\pi\eta \left(\frac{4\tilde{b} - 2\ln(\omega/\omega_0)}{(2\tilde{b} - \ln(\omega/\omega_0))^2} - \imath \frac{\pi}{(2\tilde{b} - \ln(\omega/\omega_0))^2} \right). \tag{100}$$

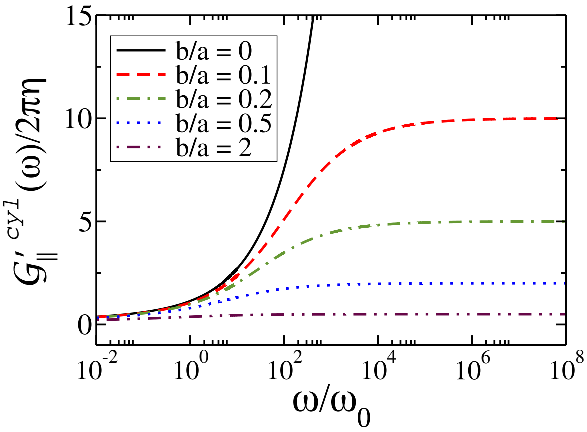

Fig. 13. (Color online) Real part of $\mathcal{G}_\parallel^{\mathrm{cyl}}(\omega)$ given by eq. (99), the response function for a cylinder oscillating parallel to its long axis for various slip lengths, $\tilde{b} = b/a$. Note that there is no dependence on the compressibility parameter γ.

The ratio of the parallel response function given above and the perpendicular response function, eq. (89), is $\mathcal{G}_\perp^{\mathrm{cyl}}/\mathcal{G}_\parallel^{\mathrm{cyl}} \simeq 2$ in the limit of $\omega \to 0$, in agreement with slender body theory [18]. On the other hand, the high-frequency behavior of $\mathcal{G}_\parallel^{\mathrm{cyl}}(\omega)$ is identical to that of a tangentially oscillating plane, eq. (53), times the cylinder circumference (for a derivation see appendix A.3).

7 Discussion and conclusion

The response of a viscous compressible fluid to the motion of a plane, a sphere and a cylinder has been calculated as a function of surface slip length and frequency using a Green's function approach. We construct the flow fields around these objects in closed form. The response functions for the sphere and cylinder display a resonant feature at a frequency $\omega^* \sim \omega_0\gamma^{1/2} = c/a$ for high enough values of the parameter γ (*i.e.* for low enough values of the compressibility), where c/a is the inverse time sound needs to travel a typical distance a corresponding to the sphere or cylinder radius. For small frequencies a distinct resonance appears roughly at the boundary between the propagating and diffusive regimes. The effect of slip on the drag force is shown to be particularly important for high frequencies.

We have defined the frequency-dependent response function $\mathcal{G}(\omega)$ (which corresponds to a frequency-dependent friction coefficient) in the linear-response limit and in the absence of inertia effects by $F_i(\omega) = \delta_{ij}\mathcal{G}(\omega)V_j(\omega)$, where $V_j(\omega)$ is the frequency-dependent particle velocity and $F_i(\omega)$ the frequency-dependent external force acting on the particle. For a particle with a finite effective mass m_0, corresponding to the particle mass minus the mass of the displaced fluid, the equation of motion reads

$$-\imath\omega m_0 V_i(\omega) + \mathcal{G}(\omega)V_i(\omega) = F_i(\omega). \tag{101}$$

This shows that the imaginary part of the response function, $\mathcal{G}''(\omega)$, acts like an —in general frequency-dependent— additional mass of the particle, while the real part of the response function, $\mathcal{G}'(\omega)$, corresponds to the frequency-dependent friction coefficient. The frequency-dependent power dissipation reads $\mathcal{P}(\omega) = \mathrm{Re}(F_i(\omega)V_i(-\omega)) = \mathcal{G}'(\omega)|V_i^2(\omega)|$, which clearly shows that dissipation is a non-linear effect that does not influence response functions on the linear level. The real and the imaginary parts of the response function can be directly measured by microrheological methods [1,2]. By external excitation of cylindrical geometries such as nanotubes or cantilevers, the slip length can be directly inferred from expressions for the response function given in eqs. (88) and (99). Since the imaginary and real parts of the response function are related via Kramers-Kronig relation, probing either the real or imaginary part is sufficient to obtain the overall response function. Alternatively, by measuring the spectral density of particle thermal fluctuations, and invoking the fluctuation-dissipation theorem, one can also infer the complete response function. Note that in driven systems non-linear effects can in principle become important and lead to deviations from our linear analysis, equilibrium measurements based on particle fluctuations are by definition in the linear-response regime. Defining the complex admittance (or frequency-dependent mobility) $\mu(\omega)$ via $V_i(\omega) = \mu(\omega)F_i(\omega)$, we obtain for a massive particle from eq. (101) the expression $\mu(\omega) = (\mathcal{G}(\omega) - \imath\omega m_0)^{-1}$. The fluctuation-dissipation relations for the position and velocity autocorrelation functions are related to the real part of the admittance by [27]

$$\int_0^\infty \mathrm{d}\tau \langle V_i(t)V_i(t+\tau)\rangle e^{\imath\omega\tau} = 3k_BT\mu'(\omega), \tag{102}$$

$$\int_0^\infty \mathrm{d}\tau \langle r_i(t)r_i(t+\tau)\rangle e^{\imath\omega\tau} = \frac{3k_BT\mu'(\omega)}{\omega^2}. \tag{103}$$

In the case of an imposed velocity V_i and coupled fluctuating force F_i, the force autocorrelation function is related to the frequency-dependent friction coefficient via

$$\int_0^\infty \mathrm{d}\tau \langle F_i(t)F_i(t+\tau)\rangle e^{\imath\omega\tau} = 3k_BT\mathcal{G}'(\omega), \tag{104}$$

where it is to be noted that, in accordance with common practice, the response function in this case is defined as $F_i(\omega) = -\mathcal{G}(\omega)V_i(\omega)$ (where $\mathcal{G}$ has the same functional form as derived in the main text). This reflects the fact that the force exerted by the fluid on the particle is on average opposed to the prescribed velocity. The real part of the admittance is related to the components of the response function by $\mu'(\omega) = \mathcal{G}'(\omega)/([\mathcal{G}'(\omega)]^2 + [\mathcal{G}''(\omega) - \omega m_0]^2)$ and thus follows straightforwardly from the expressions given in our paper.

Viscoelastic effects can be easily taken into account in various standard models, the Maxwell model couples elasticity and viscosity in series and corresponds to a viscoelastic fluid. It can be incorporated into our framework by replacing the viscosity with a frequency-dependent function

$$\eta(\omega) = \frac{\eta_0}{1 - \imath\omega\tau}, \tag{105}$$

with a similar expression for the volume viscosity [11,13,21]. The viscoelastic time scale τ has empirically been found to be close to the vorticity time scale, *i.e.* setting $\tau \simeq \omega_0^{-1}$ can be viewed as a good approximation for simple fluids, but for more complex fluids pronounced deviations are of course expected. The expression equation (105) shows that viscoelastic effects only set in at high frequencies, but at these frequencies they can drastically change the resultant behavior.

The authors would like to thank the DFG (Grant No. SFB 863) for financial support and acknowledge the Feza Gürsey Institute Istanbul for the allocation of computation time.

Appendix A.

Appendix A.1. Calculation of the line Green's function

The Green's function resulting from eq. (79) can be written in terms of integral functions $A_n(\alpha\sigma)$ defined as

$$A_n(\alpha\sigma) = \int_0^{+\infty} \frac{e^{-\alpha\sqrt{\sigma^2+z^2}}\mathrm{d}z}{(\alpha\sqrt{\sigma^2+z^2})^n} = \frac{1}{\alpha^n}\int_\sigma^{+\infty} \frac{e^{-\alpha r}\mathrm{d}r}{r^{n-1}\sqrt{r^2-\sigma^2}}$$
$$= \frac{1}{\alpha^n\sigma^{n-1}}\int_1^{+\infty} \frac{e^{-\alpha\sigma u}\mathrm{d}u}{u^{n-1}\sqrt{u^2-1}}, \tag{A.1}$$

and similar for $A_n(\lambda\sigma)$. Note that $A_1(\alpha\sigma)$ and $A_0(\alpha\sigma)$ are connected to second-order modified Bessel functions as $A_0(\alpha\sigma) = \sigma K_1(\alpha\sigma)$ and $A_1(\alpha\sigma) = K_0(\alpha\sigma)/\alpha$. Derivatives of $A_n(\alpha\sigma)$ are given by the recursion relation

$$\frac{\partial A_n(\alpha\sigma)}{\partial r_i} = -\frac{\hat{r}_i}{\sigma}\left[(n-1)A_n(\alpha\sigma) - A_{n-1}(\alpha\sigma)\right]. \tag{A.2}$$

Furthermore, A_n functions are related via

$$(n-1)A_n(\alpha\sigma) + A_{n-1}(\alpha\sigma) = \alpha^2\sigma^2[nA_{n+2}(\alpha\sigma) + A_{n+1}(\alpha\sigma)]. \tag{A.3}$$

Using eqs. (A.1) and (A.3) in eq. (80) gives the line Green's functions as

$$\begin{aligned} G_{ij}^{\mathrm{line},T}(\sigma) &= \delta_{iz}\delta_{jz}\frac{K_0(\alpha\sigma)}{2\pi\eta} \\ &\quad + \frac{\alpha}{2\pi\eta\alpha^2\sigma}\{(\delta_{ix}\delta_{jx} + \delta_{iy}\delta_{jy}) \\ &\quad \times[K_1(\alpha\sigma) + \alpha\sigma K_0(\alpha\sigma)] \\ &\quad -\hat{r}_i\hat{r}_j(\delta_{ix}\delta_{jx} + \delta_{iy}\delta_{jy} + \delta_{ix}\delta_{jy} + \delta_{iy}\delta_{jx}) \\ &\quad \times[2K_1(\alpha\sigma) + \alpha\sigma K_0(\alpha\sigma)]\}, \\ G_{ij}^{\mathrm{line},L}(\sigma) &= \frac{\lambda}{2\pi\eta\alpha^2\sigma}\{-(\delta_{ix}\delta_{jx} + \delta_{iy}\delta_{jy})K_1(\lambda\sigma) \\ &\quad +\hat{r}_i\hat{r}_j(\delta_{ix}\delta_{jx} + \delta_{iy}\delta_{jy} + \delta_{ix}\delta_{jy} + \delta_{iy}\delta_{jx}) \\ &\quad \times[2K_1(\lambda\sigma) + \lambda\sigma K_0(\lambda\sigma)]\}. \end{aligned} \tag{A.4}$$

Appendix A.2. Calculation of the cylinder response function for perpendicular motion

We start from eq. (81), where here and in the following i and j can be either x or y. To calculate the effect of the ∇^2 operator, we use the following identities:

$$\nabla^2(r_i r_j A_n) = 2\delta_{ij}A_n + \frac{r_i r_j}{\sigma^2}[(n-1)(n-5)A_n + (2n-7)A_{n-1} + A_{n-2}],$$
$$\nabla^2 A_n = \frac{1}{\sigma^2}[(n-1)^2 A_n + (2n-3)A_{n-1} + A_{n-2}]. \tag{A.5}$$

The above identities give $\nabla^2 G_{ij}^{\mathrm{line},T} = \alpha^2 G_{ij}^{\mathrm{line},T}$ and $\nabla^2 G_{ij}^{\mathrm{line},L} = \lambda^2 G_{ij}^{\mathrm{line},L}$. Using these results in eq. (81) gives

$$\begin{aligned} G_{ij}^{\mathrm{cyl},\perp}(\sigma) &= \underbrace{(D_0 + D_2 a^2\alpha^2)}_{E_1^{\mathrm{cyl}}} G_{ij}^{\mathrm{line},T} + \underbrace{(D_0 + D_2 a^2\lambda^2)}_{E_2^{\mathrm{cyl}}} G_{ij}^{\mathrm{line},L} \\ &= E_1^{\mathrm{cyl}} G_{ij}^{\mathrm{line},T} + E_2^{\mathrm{cyl}} G_{ij}^{\mathrm{line},L} \\ &= \frac{\alpha E_1^{\mathrm{cyl}}}{2\pi\eta\alpha^2\sigma}\{\delta_{ij}[K_1(\alpha\sigma) + \alpha\sigma K_0(\alpha\sigma)] - \hat{r}_i\hat{r}_j[2K_1(\alpha\sigma) + \alpha\sigma K_0(\alpha\sigma)]\} \\ &\quad + \frac{\lambda E_2^{\mathrm{cyl}}}{2\pi\eta\alpha^2\sigma}\{-\delta_{ij}K_1(\lambda\sigma) + \hat{r}_i\hat{r}_j\,[2K_1(\lambda\sigma) + \lambda\sigma K_0(\lambda\sigma)]\}. \end{aligned} \tag{A.6}$$

The coefficients E_1^{cyl} and E_2^{cyl} are determined by boundary conditions eqs. (82) and (83) at the cylinder surface. Using eqs. (A.2) and (A.3), the coefficients E_1^{cyl} and E_2^{cyl} can be written as

$$E_1^{\mathrm{cyl}} = -\frac{(2\tilde{b}+1)[2\tilde{\lambda}K_1(\tilde{\lambda}) + \tilde{\lambda}^2 K_0(\tilde{\lambda})]}{N_2M_1 - N_1M_2},$$
$$E_2^{\mathrm{cyl}} = -\frac{(2\tilde{b}+1)[2\tilde{\alpha}K_1(\tilde{\alpha}) + \tilde{\alpha}^2 K_0(\tilde{\alpha})] + \tilde{b}\tilde{\alpha}^3 K_1(\tilde{\alpha})}{N_2M_1 - N_1M_2}, \tag{A.7}$$

where the N_i and M_i coefficients, the final results for which are given in terms of Bessel functions in eq. (85), are determined in terms of the A_n functions as

$$\begin{aligned} M_1 &= -2\alpha^3\tilde{b}[2A_3(\alpha a) + 2A_2(\alpha a) + A_1(\alpha a)] - \tilde{b}\alpha^3 A_0(\alpha a) - \alpha^3[A_3(\alpha a) + A_2(\alpha a) + A_1(\alpha a)], \\ M_2 &= -\alpha^3[A_3(\alpha a) + A_2(\alpha a)], \\ N_1 &= 2\lambda^3\tilde{b}[2A_3(\lambda a) + 2A_2(\lambda a) + A_1(\lambda a)] + \lambda^3[A_3(\lambda a) + A_2(\lambda a)], \\ N_2 &= \lambda^3[A_3(\lambda a) + A_2(\lambda a) + A_1(\lambda)], \end{aligned} \tag{A.8}$$

where $\tilde{b} = b/a$. The denominator in the expressions for E_1^{cyl} and E_2^{cyl} is given by

$$\begin{aligned} N_2M_1 - N_1M_2 &= \left(\frac{2\pi\eta\tilde{\alpha}^2}{F_i/V_i^{\mathrm{cyl}}}\right)^{-1}\Big\{\tilde{\lambda}\tilde{\alpha}(2\tilde{b}+1) \\ &\times\Big[\tilde{\alpha}K_0(\tilde{\alpha})\Big(K_1(\tilde{\lambda}) + \tilde{\lambda}K_0(\tilde{\lambda})\Big) + \tilde{\lambda}K_0(\tilde{\lambda})K_1(\tilde{\alpha})\Big] \\ &+ \tilde{b}\tilde{\alpha}^3\tilde{\lambda}K_1(\tilde{\alpha})\Big(K_1(\tilde{\lambda}) + \tilde{\lambda}K_0(\tilde{\lambda})\Big)\Big\}, \end{aligned} \tag{A.9}$$

where $\tilde{\alpha} = a\alpha$ and $\tilde{\lambda} = a\lambda$.

Appendix A.3. Large-curvature limits of response functions

In the limit of $a \to \infty$, both cylindrical and spherical response functions are expected to converge towards combinations of the normal and tangential response functions obtained for a plane. This constitutes a sensitive test on the validity of our expressions.

Spherical response function: The complete response function of a spherical particle has been given in the main text by eq. (69). For $a \to \infty$, eq. (69) takes the form

$$\lim_{a\to\infty}\mathcal{G}^{sp}(\omega) \simeq \frac{4\pi\eta a^2}{3}\frac{\lambda\alpha^2 + b\alpha^3\lambda + 2\lambda^2\alpha}{\lambda^2(b\alpha+1)},$$

and after some simplifications, the above equation turns into

$$\lim_{a\to\infty}\mathcal{G}^{sp}(\omega) \simeq 4\pi a^2\left(\frac{1}{3}\frac{\alpha^2\eta}{\lambda} + \frac{2}{3}\frac{\alpha\eta}{b\alpha+1}\right). \tag{A.10}$$

This shows that the response of a sphere in the infinite-radius limit, $a \to \infty$, is the weighted combination of the normal and the tangential planar response functions given in eqs. (47) and (53) times the area of a sphere. Indeed, at an infinitely large sphere, the vectorial force $\boldsymbol{f}$ acting on each surface element can be considered as a combination of normal and tangential components,

$$f_j = \frac{\alpha^2\eta}{\lambda}V_i^{sp}\hat{r}_i\hat{r}_j + \frac{\alpha\eta}{b\alpha+1}V_i^{sp}(\delta_{ij} - \hat{r}_i\hat{r}_j), \tag{A.11}$$

where V_i^{sp} is the sphere velocity. Integration of this force over the spherical surface corresponds to

$$\overline{f_i} = \int \mathrm{d}r^3 f_i\delta(|r| - a), \tag{A.12}$$

which straightforwardly leads to eq. (A.10).

Cylindrical response function: The same analysis can be done for the parallel and the perpendicular response functions of the cylinder. The parallel component of the cylinder response function has been given in eq. (99) as

$$\mathcal{G}_{\parallel}^{\mathrm{cyl}} = 2\pi\eta\frac{\alpha K_1(\alpha a)}{b\alpha K_1(\alpha a) + K_0(\alpha a)}.$$

As $a \to \infty$, this equation crosses over to

$$\lim_{a\to\infty} \mathcal{G}_{\parallel}^{\rm cyl} = 2\pi\eta \frac{\alpha a K_1(\alpha a)}{K_1(\alpha a)(b\alpha + K_0(\alpha a)/K_1(\alpha a))} \simeq 2\pi a \frac{\alpha\eta}{b\alpha+1} \quad (A.13)$$

and thus equals the tangential response function of a plane, eq. (53), times the circumference of the cylinder.

The perpendicular component of the cylinder response function can be treated similarly. Using the asymptotic behavior of the Bessel functions, $\lim_{x\to\infty} K_n(x) \simeq \frac{e^{-x}}{\sqrt{x}}$, the coefficients in eq. (85) follow as

$$\lim_{a\to\infty} M_1 \simeq \frac{-\alpha^2 e^{-a\alpha}}{\sqrt{\alpha a}} - \frac{b\alpha^3 e^{-a\alpha}}{\sqrt{\alpha a}}, \quad \lim_{a\to\infty} M_2 \simeq 0, \quad \lim_{a\to\infty} N_1 \simeq 0, \quad \lim_{a\to\infty} N_2 \simeq \frac{\lambda^2 e^{-\lambda a}}{\sqrt{\lambda a}},$$

and yield in the limit $a \to \infty$

$$E_1^{\rm cyl} \simeq \frac{2\pi\eta}{F_i/V_i^{\rm cyl}} e^{\alpha a} \frac{\sqrt{\alpha a}}{b\alpha+1}, \quad E_2^{\rm cyl} \simeq \frac{2\pi\eta\alpha^2}{F_i/V_i^{\rm cyl}} e^{\lambda a} \frac{\sqrt{\lambda a}}{\lambda^2}. \quad (A.14)$$

Substitution of these coefficients into eq. (88) gives the final form of the cylindrical response function in the infinite radius limit as

$$\lim_{a\to\infty} \mathcal{G}_{\perp}^{\rm cyl}(\omega) \simeq 2\pi a \left(\frac{1}{2}\frac{\alpha^2\eta}{\lambda} + \frac{1}{2}\frac{\alpha\eta}{b\alpha+1}\right), \quad (A.15)$$

which is again a weighted average of the tangential and normal planar response functions over the cylinder surface times the cylinder circumference.

Appendix A.4. Incompressible limit for cylinders

Analytical expressions for the response function of a cylinder in an incompressible non-steady flow field have been given by various authors [23]. The limit of an incompressible fluid can be obtained from our more general results by taking the limit of $\lambda \to 0$ and constitutes another test of our results. Suppose that the cylinder oscillates in the x-direction with a frequency-dependent velocity $V_x^{\rm cyl}$. From eq. (A.6) one can calculate $v_x^\perp$ and $v_y^\perp$ with the no-slip condition by using $G_{xx}^{\rm cyl,\perp}$ and $G_{xy}^{\rm cyl,\perp}$. The velocity components can be explicitly written as

$$v_x^\perp(\sigma,\phi) = V_x^{\rm cyl}\left[\frac{2}{\alpha\sigma}A - \cos\phi^2 B + \frac{a}{\alpha\sigma^2}(2\cos\phi^2 - 1)C\right],$$
$$v_y^\perp(\sigma,\phi) = V_x^{\rm cyl}\sin\phi\cos\phi\left[-\frac{2}{\alpha\sigma}B + \frac{2a}{\alpha\sigma^2}C\right],$$

where

$$A = \frac{K_1(\alpha\sigma)}{K_0(\alpha a)} + \alpha\sigma\frac{K_0(\alpha\sigma)}{K_0(\alpha a)}, \quad B = \frac{2K_1(\alpha\sigma)}{K_0(\alpha a)} + \alpha\sigma\frac{K_0(\alpha\sigma)}{K_0(\alpha a)}, \quad C = \frac{2K_1(\alpha a)}{K_0(\alpha a)} + \alpha a, \quad (A.16)$$

with the angle ϕ defined in fig. 6. Since $v_\sigma^\perp = v_x^\perp\cos\phi + v_y^\perp\sin\phi$ and $v_\phi^\perp = -v_x^\perp\sin\phi + v_y^\perp\cos\phi$, the velocity components in cylindrical components read as

$$v_\sigma^\perp(\sigma,\phi) = V_x^{\rm cyl}\cos\phi\left[\frac{a^2}{\sigma^2} - \frac{2K_1(\alpha\sigma)}{\alpha\sigma K_0(\alpha a)} + \frac{2aK_1(\alpha a)}{\alpha\sigma^2 K_0(\alpha a)}\right],$$
$$v_\phi^\perp(\sigma,\phi) = V_x^{\rm cyl}\sin\phi \times\left[\frac{a^2}{\sigma^2} - \frac{2K_0(\alpha\sigma)}{K_0(\alpha a)} - \frac{2K_1(\alpha\sigma)}{\alpha\sigma K_0(\alpha a)} + \frac{2aK_1(\alpha a)}{\alpha\sigma^2 K_0(\alpha a)}\right] \quad (A.17)$$

and agree with the expressions derived previously in the incompressible limit [23].

References

1. F. Ziemann, J. Rädler, E. Sackmann, Biophys. J. **66**, 2210 (1994).
2. F. Amblard, A.C. Maggs, B. Yurke, A.N. Pargellis, S. Leibler, Phys. Rev. Lett. **77**, 4470 (1996).
3. T.G. Mason, D.A. Weitz, Phys. Rev. Lett. **74**, 1250 (1995).
4. T.G. Mason, K. Ganesan, J.H. van Zanten, D. Wirtz, S.C. Kuo, Phys. Rev. Lett. **79**, 3282 (1997).
5. F. Gittes, B. Schnurr, P.D. Olmsted, F.C. MacKintosh, C.F. Schmidt, Phys. Rev. Lett. **79**, 3286 (1997).
6. M.L. Gardel, M.T. Valentine, J.C. Crocker, A.R. Bausch, D.A. Weitz, Phys. Rev. Lett. **91**, 158302 (2003).
7. N. Cappallo, C. Lapointe, D.H. Reich, R.L. Leheny, Phys. Rev. E **76**, 031505 (2007).
8. K. Moloni, M.R. Buss, R.P. Andres, Ultramicroscopy **80**, 237 (1999).
9. C. Li, T.W. Chou, Appl. Phys. Lett. **84**, 5246 (2004).
10. W. Zhang, K.L. Turner, Sens. Actuators A **134**, 594 (2006).
11. R. Zwanzig, M. Bixon, Phys. Rev. A **2**, 2005 (1970).
12. D. Bedeaux, P. Mazur, Physica **78**, 505 (1974).
13. H. Metiu, D.W. Oxtoby, K.F. Freed, Phys. Rev. A **15**, 361 (1977).
14. D.M. Huang, C. Sendner, D. Horinek, R.R. Netz, L. Bocquet, Phys. Rev. Lett. **101**, 226101 (2008).
15. J.H. Walther, T. Werder, R.L. Jaffe, P. Koumoutsakos, Phys. Rev. E **69**, 062201 (2004).
16. W. Tang, S.G. Advani, J. Chem. Phys. **125**, 174706 (2006).
17. G.G. Stokes, Proc. Cambridge Philos. Soc. **9**, 8 (1851).
18. S. Kim, S. Karrila, *Microhydrodynamics* (Dover, 2005).
19. A.N. Guz, Int. Appl. Math. **29**, 12 (1993).

20. P. Espanol, Physica A **214**, 185 (1995).
21. B.U. Felderhof, J. Chem. Phys. **123**, 044902 (2005).
22. B.U. Felderhof, J. Chem. Phys. **123**, 184903 (2005).
23. J. Holtsmark *et al.*, J. Acoust. Soc. Am. **26**, 26 (1953).
24. C.-Y. Wang, J. Fluid Mech. **32**, 55 (1967).
25. H. Diamant, J. Phys. Soc. Jpn. **78**, 041002 (2009).
26. D. Long, A. Ajdari, Eur. Phys. J. E **9**, 29 (2001).
27. S.R. de Groot, P. Mazur, *Non-Equilibrium Thermodynamics* (North-Holland Publishing Company, Amsterdam, 1962).